Combined atomistic-continuum modeling of short-pulse laser melting and disintegration of metal films

Dmitriy S. Ivanov and Leonid V. Zhigilei*

Department of Materials Science and Engineering, University of Virginia, 116 Engineer's Way, Charlottesville, Virginia 22904-4745, USA

The kinetics and microscopic mechanisms of laser melting and disintegration of thin Ni and Au films irradiated by a short, from 200 fs to 150 ps, laser pulse are investigated in a coupled atomistic-continuum computational model. The model provides a detailed atomic-level description of fast nonequilibrium processes of laser melting and film disintegration and, at the same time, ensures an adequate description of the laser light absorption by the conduction band electrons, the energy transfer to the lattice due to the electron-phonon coupling, and the fast electron heat conduction in metals. The interplay of two competing processes, the propagation of the liquid-crystal interfaces (melting fronts) from the external surfaces of the film and homogeneous nucleation and growth of liquid regions inside the crystal, is found to be responsible for melting of metal films irradiated by laser pulses at fluences close to the melting threshold. The relative contributions of the homogeneous and heterogeneous melting mechanisms are defined by the laser fluence, pulse duration, and the strength of the electron-phonon coupling. At high laser fluences, significantly exceeding the threshold for the melting onset, a collapse of the crystal structure overheated above the limit of crystal stability takes place simultaneously in the whole overheated region within $\sim$2 ps, skipping the intermediate liquid-crystal coexistence stage. Under conditions of the inertial stress confinement, realized in the case of short $\tau \lesssim 10$ ps laser pulses and strong electron-phonon coupling (Ni films), the dynamics of the relaxation of the laser-induced pressure has a profound effect on the temperature distribution in the irradiated films as well as on both homogeneous and heterogeneous melting processes. Anisotropic lattice distortions and stress gradients associated with the relaxation of the laser-induced pressure destabilize the crystal lattice, reduce the overheating required for the initiation of homogeneous melting down to $T \approx 1.05 T_m$, and expand the range of pulse durations for which homogeneous melting is observed in 50 nm Ni films up to $\sim$150 ps. High tensile stresses generated in the middle of an irradiated film can also lead to the mechanical disintegration of the film.

I. INTRODUCTION

Short-pulse laser interaction with metals is a subject of practical as well as fundamental scientific interest. Practical applications range from well-established methods for surface processing[1] and pulsed laser deposition of thin films and coatings[2] to the emerging new areas such as microfabrication of nanostructures with resolutions exceeding the optical diffraction limit.[3] Further optimization of experimental parameters in current applications and the emergence of new techniques can be facilitated by a better theoretical understanding of the relation between the basic mechanisms of laser interaction with materials, nonequilibrium processes caused by the fast deposition of laser energy, and the resulting microstructure and properties of the materials treated by laser irradiation.

From the point of view of fundamental science, short-pulse laser irradiation has the ability to bring material into a highly nonequilibrium state and provides unique insights into material behavior under extreme conditions that can hardly be achieved by any other means. Analysis of the laser-induced processes leads to a range of important fundamental questions, such as the limit of superheating, the microscopic mechanisms of homogeneous and heterogeneous melting, and the nature of the fracture/spallation at ultrahigh deformation rates and elevated temperatures, as well as the mechanisms of explosive boiling and disintegration of material in laser ablation.

The focus of the present paper is the microscopic analysis of the mechanisms of short-pulse laser melting. Although melting is a common and well-studied phenomenon, the nature of the structural instability of a superheated crystal and the microscopic mechanisms of melting are still subjects of active scientific discussions.[4–10] It has been well established that melting starts at surfaces and internal crystal defects under rather minor superheating conditions or even below the equilibrium melting temperature.[6,7,11–14] The later effect of surface premelting is related to the lower free energy of the surface wetted by a thin liquid layer as compared to the ordered solid surface. After heterogeneous nucleation of the liquid phase, the liquid-solid interface propagates into the bulk of the solid, precluding any significant overheating. It is this barrierless (or almost barrierless) nucleation of the liquid phase at the surface that makes observation of an alternative mode of melting, homogeneous nucleation in the bulk of a superheated crystal, difficult.

Short-pulse laser irradiation combined with new optical, x-ray, and electron diffraction time-resolved probe techniques[15–22] has a promise of providing new insights into the mechanisms and kinetics of ultrafast phase transformations. The extremely high heating rates of 10^{14} K/s and even more can be achieved by ultrashort-pulse (pico- and femtosecond) laser irradiation, opening unique opportunities for investigation of the kinetic limits of achievable superheating. Experimental investigations of the ultrafast phase transformations in metals and semiconductors[15–22] performed by

68 064114-1

various time-resolved pump-probe techniques suggest that, depending on the irradiation conditions and properties of the material, the melting of the surface layer can take from several picoseconds to nanoseconds. The melting time of several hundreds of picoseconds and longer[15,17,20] is consistent with a conventional picture of heterogeneous nucleation of the liquid phase at the irradiated surface and propagation of the melting front deeper into the bulk of the crystal.[23] A typical thickness of the layer affected by the ultrashort laser heating is on the order of 100 nm for metals or semiconductors, whereas the velocity of the melting front propagation has a strong dependence on the degree of superheating, but is limited by the speed of sound.[24] The melting time of several picoseconds[15,18,19,21,22] is too short to be explained by the heterogeneous melting mechanism, and the melting can be attributed to homogeneous nucleation of the liquid phase inside the superheated surface region. Therefore, depending on the irradiation condition, optical and thermal properties of the material, and the time of the electron-phonon equilibration in the system, the dynamics of laser melting is defined by propagation of the melting front from the surface and/or homogeneous nucleation of the liquid phase in the bulk of the superheated crystal.[25]

In this paper we present the result of a computational study of the microscopic mechanisms of laser melting of thin nickel and gold films irradiated by short, from 200 fs to 150 ps, laser pulses. Computational models that can be applied for the description of laser-metal interactions at the continuum and atomic level are critically reviewed next, in Sec. II. A hybrid computational approach that combines atomistic molecular dynamics simulations with a continuum description of the laser excitation and subsequent relaxation of the conduction band electrons is described in Sec. III. Parameters of the systems used in the simulations are given in Sec. IV, and the simulation results are presented in Secs. V and VI for nickel and gold films, respectively. An overall picture of laser melting and disintegration of thin metallic films emerging from the simulations is briefly reviewed in Sec. VII.

II. COMPUTATIONAL DESCRIPTION OF SHORT-PULSE LASER INTERACTION WITH METALS

In metals, laser light is absorbed by the conduction band electrons. The deposited energy quickly, within femtoseconds, is equilibrated among the electrons and, more slowly, is transferred to the atomic vibrations. The latter process is controlled by the strength of the electron-phonon coupling and can take from a fraction of a picosecond to several tens of picoseconds. Finally, a thermal equilibrium is established between the electrons and phonons, and the heat flow from the surface region into the bulk of the irradiated target can be described as the common thermal diffusion. When the laser pulse duration is comparable or less than the time needed for electron-phonon thermalization, a state of thermal nonequilibrium is created by laser irradiation, with electrons and lattice having different temperatures. At the continuum level, the time evolution of the lattice and electron temperatures, T_l and T_e, can be described within a so-called two-temperature

model[26,27] (TTM) by two coupled nonlinear differential equations,

$$C_e(T_e)\frac{\partial T_e}{\partial t} = \nabla[K_e(T_e)\nabla T_e] - G(T_e - T_l) + S(z,t), \quad (1)$$

$$C_l(T_l)\frac{\partial T_l}{\partial t} = \nabla[K_l(T_l)\nabla T_l] + G(T_e - T_l), \quad (2)$$

where C and K are the heat capacities and thermal conductivities of the electrons and lattice as denoted by subscripts e and l, and G is the electron-phonon coupling constant. The source term $S(z,t)$ is used to describe the local laser energy deposition per unit area and unit time during the laser pulse duration. In Eq. (2) a term responsible for the phonon heat conduction is typically negligible as compared to the electron heat conduction in metals and is often omitted. The system of Eqs. (1) and (2) can be solved by a finite difference method and the spatial and time evolution of the electron and lattice temperatures can be obtained.

As an illustration of the model predictions, the temperature profiles for a 50 nm Ni film irradiated by a 200 fs laser pulse are shown in Fig. 1(a) for the front and rear surfaces of the film. We can see that equilibration between the hot electrons and the lattice takes up to 20 ps for the Ni film, and the heating rate as well as the energy distribution in the film is strongly affected by the equilibration kinetics. A simple description of melting is also included in the model by tracking the fraction of the melted material in any finite difference discretization cell where the equilibrium melting temperature is reached and taking away the latent heat of melting until the complete melting is reached. The melting process is reflected in regions of the constant-temperature plateau in the lattice temperature profiles. The model predicts that melting of the front surface region starts at ~3 ps after the laser pulse and takes ~4 ps, whereas melting of the back surface region starts at ~8 ps after the laser pulse and takes ~12 ps. As will be shown in Sec. V, these predictions on the melting kinetics are very different from the predictions of a more realistic model in which overheating and the effect of pressure on the melting process are included.

Over the last 30 years, TTM has become the main model to describe the kinetics of the electron and lattice temperature evolution in a metal target irradiated with a short laser pulse. In conjunction with pump-probe measurements of transient changes in surface reflectance, TTM has been used to obtain information on the thermal conductivity, the electron-phonon coupling constants,[28–33] mechanical properties of thin films,[30] and the effect of grain boundaries[34,35] and small size of the system[36,37] on the electron-phonon relaxation. The model has also been used to predict the threshold fluences for the onset of laser damage/melting[38] and laser-induced desorption of species from metal surfaces,[39] as well as to explain the dynamics of ion ejection in laser ablation.[40] Despite the successful applications and popularity of TTM, the model has a number of inherent limitations. Some of the limitations can be overcome by adding "more physics" within the framework provided by TTM. In particular, recent developments include incorporation, through the parameters
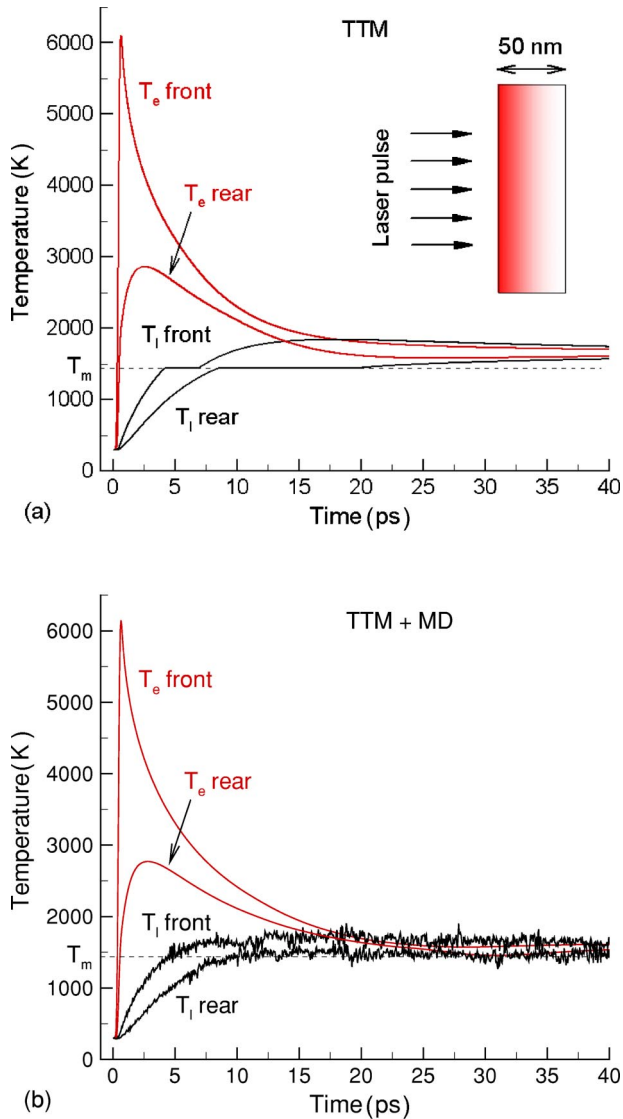
FIG. 1. (Color online) Time dependence of electron and lattice temperatures predicted by (a) the TTM and (b) combined TTM-MD methods for a 50 nm Ni film irradiated with a 200 fs laser pulse at an absorbed fluence of 430 J/m^2. The values of the melting temperature and the latent heat of melting determined for the EAM Ni material are used in the TTM calculation (a). Dashed lines show the melting temperature of the EAM Ni.

of TTM, of the description of the surface and grain boundary scattering,[41] as well as the energy transfer by ballistic electrons,[32,33,42] combining TTM with the hot electron blast model[43] and thermoelasticity equations to investigate the conditions for nonthermal damage to thin metal films.[44]

Other limitations are harder to overcome within a continuum model. In particular, the description of phase transformations occurring under highly nonequilibrium conditions induced in the target material by short-pulse laser irradiation is difficult at the continuum level and typically involves a number of assumptions and simplifications. Part of the problem is that the physics of ultrafast phase transformations and damage occurring under highly nonequilibrium conditions is not well understood and therefore cannot be reliably de-scribed by a set of kinetic equations. Even the basic questions on the kinetics and microscopic mechanisms of melting and boiling under conditions of strong overheating continue to remain the subjects of active scientific debates. In particular, at the extremely high levels of superheating realized in ultrashort-pulse laser melting, when the melting front propagation is approaching the speed of sound and the size of a critical nucleus becomes comparable to several interatomic distances, the applicability of macroscopic kinetic approaches based on classical nucleation theory[5,10,23] is questionable and should be verified by a detailed microscopic analysis of the involved processes. Similarly, the processes leading to material ejection and plume formation in short-pulse laser ablation are not well established, with Coulomb explosion,[45] explosive homogeneous boiling,[46–48] and spin-odal decomposition[49,50] of the material overheated by a short laser pulse being discussed as possible mechanisms responsible for the ablation onset.

A computational method that is suitable for simulation of fast nonequilibrium processes and therefore can provide insights into the mechanisms of laser-metal interactions is the molecular dynamics (MD) method. The advantage of the MD method is that only details of the interatomic interaction need to be specified, and no assumptions are made about the character of the processes under study. In particular, MD has been demonstrated to be an efficient tool for a microscopic analysis of the melting mechanisms under conditions of overheating in both the bulk of a crystal[8,51,52] and in systems with a free surface.[53,54] Simulations of boiling, spinodal de-composition and fragmentation of a metastable liquid,[55–57] generation and propagation of laser-induced pressure waves,[58,59] and laser ablation[60–63] has been also reported. The classical MD method, however, is not directly applicable for simulation of laser interactions with metals. Since the electronic contribution to the thermal conductivity of a metal is dominant, the conventional MD method, where only the lattice contribution is present, significantly underestimates the total thermal conductivity. This leads to unphysical confinement of the deposited laser energy in the surface region of the irradiated target and does not allow for direct comparison between the calculated and experimental data. Moreover, the laser energy absorption by the conduction band electrons and the transient state of electron-lattice nonequilibrium cannot be reproduced since the electrons are not explicitly represented in the model. A computational model aiming at overcoming these limitations and combining the advantages of TTM and MD for a realistic description of the diverse range of processes induced by short-pulse laser irradiation of a metal target is described below.

III. COMBINED TTM-MD MODEL

In the combined method the MD method completely substitutes the TTM equation for the lattice temperature, Eq. (2). The diffusion equation for electron temperature T_e, Eq. (1), is solved by a finite difference method simultaneously with MD integration of the equations of motion of atoms and the electron temperature enters the coupling term,[54,64,65] which is

DMITRIY S. IVANOV AND LEONID V. ZHIGILEI

PHYSICAL REVIEW B **68**, 064114 (2003)

responsible for the energy exchange between the electrons and the lattice,

$$C_e(T_e)\frac{\partial T_e}{\partial t} = \frac{\partial}{\partial z}\left(K_e(T_e)\frac{\partial}{\partial z}T_e\right) - G(T_e - T_l)$$
$$+ S(z,t), \quad \text{TTM} \tag{3}$$

$$m_i\frac{d^2\mathbf{r}_i}{dt^2} = \mathbf{F}_i + \xi m_i\mathbf{v}_i^T, \quad \text{MD}$$

where

$$\xi = \frac{1}{n}\sum_{k=1}^{n} GV_N(T_e^k - T_l) \bigg/ \sum_i m_i(\mathbf{v}_i^T)^2. \tag{4}$$

Since in short-pulse laser irradiation the laser spot size is typically much larger as compared to the depth affected by the laser heating, a one-dimensional version of the diffusion equation for electron temperature, Eq. (1), is used here.

In Eq. (4), m_i and $\mathbf{r}_i$ are the mass and position of an atom i, and $\mathbf{F}_i$ is the force acting on atom i due to the interatomic interaction. An additional term, added to the ordinary MD equations of motion, accounts for the electron-phonon coupling. A modified, as compared to earlier works,[54,65] formulation of the coupling term is used in the model (see Appendix A). The new formulation distinguishes between the thermal velocities of the atoms, $\mathbf{v}_i^T$, and the velocities of their collective motion. It also does not require *a priori* knowledge of the lattice heat capacity of the model system, which is, in general, a function of temperature (see Sec. V A). Cells in the finite difference discretization are related to the corresponding volumes in the MD system. The lattice temperature and coefficient ξ are defined for each cell of a volume V_N, and the summation Σ_i in Eq. (4) is performed over all the atoms in a given cell. The expansion, density variations along the z axes, and, at higher fluences, disintegration of the irradiated target predicted in the MD part of the model are accounted for in the continuum part of the model. New cells are activated when the number of atoms in the corresponding MD regions exceeds a certain critical number, taken in this work to be 10% of the average number of atoms in a cell in the initial system. Cells are deactivated when the number of atoms in the corresponding MD region falls below the critical number. The atoms in the deactivated cells are included in the nearest active cell if they are located within a distance equal to a half the size of a cell from the active cell.

The step of the spatial discretization in the finite difference (FD) integration of Eq. (3) can be estimated based on the von Neumann stability criterion, $\Delta t_{FD} \leq 0.5(\Delta x_{FD})^2 C_e(T_e)/K_e(T_e,T_l)$, for the values of the heat capacity and thermal conductivity giving the smallest time step. The maximum time step that can be used in the finite difference integration is typically smaller than the values of the time step used in the integration of the MD equations of motion, Eq. (4). Therefore, the time steps in the two parts of the combined model are chosen so that one MD time step would correspond to an integer number of finite difference

time steps, $\Delta t_{MD} = n\Delta t_{FD}$. In each finite difference discretization cell, the energy transferred between the electrons and the lattice due to the electron-phonon coupling is accumulated for n steps of integration,

$$\Delta E^{e\text{-ph}} = \sum_{k=1}^{n} \Delta t_{FD}GV_N(T_e^k - T_l).$$

The accumulated energy is then transferred to (or extracted from) the energy of the atomic motion in the corresponding part of the MD system by means of the coupling term added to the MD equations of motion, Eq. (4), as explained in Appendix A. Note that although a smaller time step is used in the finite difference integration, the computational efficiency of the combined TTM-MD model is defined almost entirely by the MD part.

A Gaussian temporal profile is used in the simulations to describe the laser energy deposition,

$$S(z,t) = I_0(1-R)L_p^{-1}\exp(-z/L_p)\exp[-(t-t_0)^2/2\sigma^2], \tag{5}$$

where I_0 is the peak intensity, R is the reflectivity, L_p is the optical absorption depth, and σ is the standard deviation of the Gaussian profile, related to the pulse duration as $\tau_L = (\text{full width at half maximum}) = \sigma\sqrt{8\ln(2)}$. The laser fluence F is related to the peak intensity I_0 as $F = \sqrt{\pi/4\ln(2)}\tau_L I_0 \approx 1.0645\tau_L I_0$. The absorbed laser fluence, related to the incident fluence as $F_{abs} = F(1-R)$, is used in the discussion of the simulation results in this paper.

In addition to the diffusive electron energy transport assumed in TTM, Eqs. (1) and (3), the ballistic motion of the excited electrons can significantly alter the initial energy deposition depth for s/p-band metals, where the electron-electron collision rate is relatively small. Before the excited electrons equilibrate due to collisions with other electrons near the Fermi level and form a Fermi distribution with a certain electron temperature, they can propagate from the optical absorption depth deeper into the bulk of the irradiated sample with velocities close to the Fermi velocity, $\sim 10^6$ m/s. This ballistic motion of the excited electrons leads to the fast, within ~ 100 fs redistribution of the deposited energy within the ballistic range that is defined by the mean free path of the electrons. It has been suggested[32,38,42] that the effect of ballistic electrons can be incorporated into TTM by substituting the optical penetration depth L_p in the source term, Eq. (5), by an effective laser energy deposition depth defined by both optical absorption and ballistic energy transport, $L_p + L_b$, where L_b is the ballistic range. An additional correction should be introduced in the source term for system with sizes comparable to the effective energy deposition depth.[32,38,42]

The energy exchange between the two parts of the combined model is schematically illustrated in Fig. 2. In the case of a bulk sample irradiated by a laser pulse,[54,65] the MD method is used only in a topmost surface region of the target, where active processes of laser melting and ablation are taking place, whereas the diffusion equation for electron temperature is solved in a much wider region affected by the
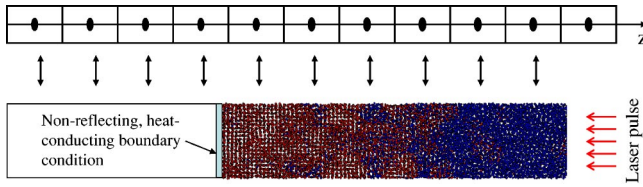
064114-4

FIG. 2. (Color online) Schematic representation of the combined continuum-atomistic model. The evolution of the electron temperature is described by a nonlinear differential equation [Eq. (3)], whereas the atomic motions are described by the MD method with additional forces that account for the energy exchange due to the electron-phonon coupling [Eq. (4)]. Spatial discretization in the continuum model (typically ~1 nm) and size of the atomistic region are not drawn to scale. Nonreflecting boundary conditions are described in Refs. 58 and 79.

thermal conduction from the absorbing surface layer. In order to avoid reflection of the pressure waves propagating from the irradiated surface, the dynamic boundary condition that mimics the interaction of the atoms in the boundary region with the outer ''infinite elastic medium'' [58] should be applied at the bottom of the MD region. Simulations presented in this paper are performed for free-standing thin metal films and free boundary conditions are applied at both surfaces of the film. Periodic boundary conditions are imposed in the directions parallel to the free surfaces. These conditions simulate the situation in which the laser spot diameter is large compared to the depth of the laser energy deposition so that the effects of the edges of the laser beam can be neglected.

The hybrid approach, briefly described above, combines the advantages of the two-temperature model and the MD method. The two-temperature model provides an adequate description of the laser energy absorption in the electronic system, energy exchange between the electrons and phonons, and fast electron heat conduction in metals, whereas the MD method is appropriate for simulation of nonequilibrium processes of lattice superheating, melting, and ablation. In this paper we apply the model for investigation of the microscopic mechanisms of laser melting and disintegration of thin metal films. Parameters of the systems used in the simulations are described below.

IV. COMPUTATIONAL SETUP FOR SIMULATIONS OF LASER INTERACTION WITH THIN Ni AND Au FILMS

Simulations presented in this paper are performed for 50 nm Ni and Au free-standing films irradiated with laser pulses of different pulse widths, from 200 fs up to 200 ps. The two target materials are chosen to investigate the effect of the strength of electron-phonon coupling on laser-induced processes. The rate of the energy transfer from hot electrons to the lattice is much slower in Au as compared to Ni and, at the same time, the depth affected by the ballistic energy transport is significantly larger in Au. Since the effective laser energy deposition depth in Au is estimated to be larger than 100 nm,[32] a uniform energy deposition throughout the 50 nm Au film is used in the simulations. A theoretical pre-

diction of a uniform rise of the electronic temperature for thicknesses smaller than the ballistic range has been confirmed in a series of pump-probe measurements of transient reflectivity performed for Au films of different thicknesses, from 10 nm up to 500 nm.[33] The reflectivity changes are consistent with the assumption of a homogeneous electronic temperature increase for films with thicknesses of 100 nm or less. The effect of ballistic energy transport is negligible in Ni, and the source term, Eq. (5), with the optical penetration depth of 13.5 nm is used in the simulations of laser irradiation of Ni films.

The range of laser fluences used in the simulations is chosen so that the lowest fluence would be close to the threshold for the complete melting of the irradiated film, whereas the highest fluence would lead to disintegration of the film. Thus, the range of absorbed fluences, $F_{abs} = (1-R)F$, is from 430 J/m^2 to 1117 J/m^2 for Ni films and from 130 J/m^2 to 955 J/m^2 for Au films.

The material constants used in the description of the electron subsystem, Eq. (3), are as follows.[32] For Ni, $C_e = \gamma T_e$ with $\gamma = 1065$ J m^{-3} K^{-2}, $K_e = K_0 T_e / T_l$ with $K_0 = 91$ W m^{-1} K^{-1}, $G = 3.6 \times 10^{17}$ W m^{-3} K^{-1}. For Au $C_e = \gamma T_e$ with $\gamma = 71$ J m^{-3} K^{-2}, $G = 2.1 \times 10^{16}$ W m^{-3} K^{-1}. An expression used to describe the dependence of the electron thermal conductivity K_e on the electron and lattice temperatures in Au as well as justification of the choice of the approximations used for Ni and Au are given in Appendix B.

All the thermal and elastic properties of the lattice, such as the lattice heat capacity, elastic moduli, the coefficient of thermal expansion, melting temperature, volume and entropy of melting and vaporization, as well as the dependence of these characteristics on temperature and pressure, are defined by the interatomic interaction, described in this work by the embedded-atom method (EAM) in the form and parametrization suggested by Johnson and co-workers.[66] A series of liquid-crystal coexistence simulations are performed to determine the pressure dependence of the equilibrium melting temperature, whereas a series of constant-pressure–constant-temperature simulations are used to determine the equations of state of the model materials (see Secs. V and VI).

The initial MD system used in the simulations of laser irradiation of Ni films is an fcc crystal composed of 56 800 atoms with dimensions $3.53 \times 3.53 \times 50.14$ nm and periodic boundary conditions imposed in the directions parallel to two (100) free surfaces. A similar computational cell is used for Au (100) films, with 48 800 atoms and dimensions of $4.09 \times 4.09 \times 49.92$ nm. Before applying laser irradiation, all systems are equilibrated at 300 K.

The result of the application of the combined TTM-MD method to a 50 nm Ni film is shown in Fig. 1(b). While the temperature profiles are similar in Figs. 1(a) and 1(b), the MD description gives a much more realistic representation of the lattice response to laser heating, including thermal expansion, overheating, melting, and disintegration, as discussed in the following sections. The size of the relative temperature fluctuations in Fig. 1(b) is determined by the number of atoms in cells within the MD system, for which temperature is calculated, $\sqrt{\langle (\Delta T)^2 \rangle}/\langle T \rangle \sim 1/\sqrt{N_{cell}}$.[67] The size of the fluc-
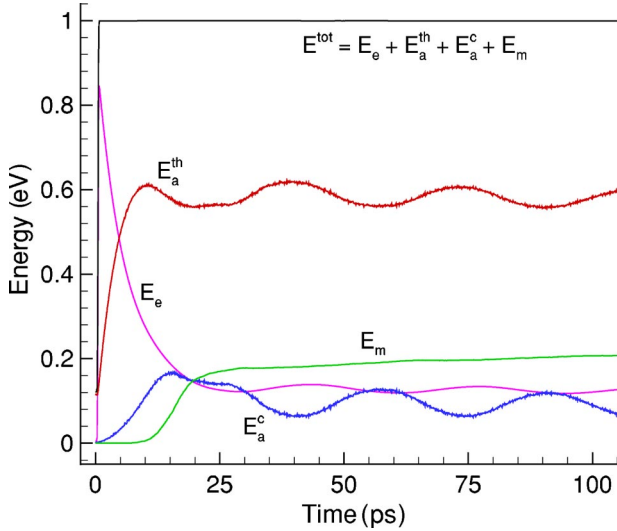
FIG. 3. (Color online) Energy redistribution in a 50 nm Ni film irradiated with a 200 fs laser pulse at an absorbed fluence of 430 J/m^2. The thermal energies of the electrons, E_e, and the atoms, E_a^{th}, the energy of the collective atomic motion due to the elastic vibrations of the film, E_a^c, the energy that went to the latent heat of melting, E_m, and the total energy of the system, $E^{tot} = E_e + E_a^{th} + E_a^c + E_m$ are shown. Energies are normalized to the total energy absorbed by the film, $E^{tot} = F_{abs}S$, where S is the surface area of the MD system and F_{abs} is the absorbed laser fluence.

tuations can be reduced by increasing the lateral size of the MD system or the step of spatial discretization used in the finite difference integration of Eq. (3), Fig. 2. The step of spatial discretization used in this work is $\Delta x_{FD} = 1$ nm, and the average number of atoms in a cell is 1159 and 996 for the initial Ni and Au films, respectively.

The time step in the finite difference integration of Eq. (3), $\Delta t_{FD} = 1.25$ fs for Ni and $\Delta t_{FD} = 0.025$ fs for Au, and the time step in the integration of the MD equations of motion, Eq. (4), $\Delta t_{MD} = 2.5$ fs, are chosen so that the von Neumann stability criterion and the synchronization requirement $\Delta t_{MD} = n\Delta t_{FD}$ are satisfied, and the total energy in the combined model is conserved with the maximum energy drift of less than 0.3% during any of the simulations discussed in this paper. The energy balance in a combined TTM-MD simulation is illustrated in Fig. 3 for the simulation, for which the surface temperatures are shown in Fig. 1(b). The total energy of the entire system is shown along with contributions from the thermal energy of the electrons, E_e, the energy (kinetic and potential) associated with the thermal motion of the atoms, E_a^{th}, the energy (kinetic and potential) of the collective atomic motion due to the elastic vibrations of the film induced by the fast laser energy deposition, E_a^c, and the energy that goes to the latent heat of melting, E_m. Both E_a^{th} and E_a^c include contributions from the kinetic and potential energies of the MD system, and the approximate separation of the MD energy into the energies of the thermal and collective motion is based on the virial theorem.[68] The energy spent on melting is determined by multiplying the fraction of the liquid phase in the system at any given time by the latent heat of melting of the model material. The fraction of the liquid

phase is determined based on the local order parameter, defined in Appendix C, whereas the latent heat of melting is calculated from the internal energy plots, Fig. 6, as discussed in Sec. V B. Figure 3 shows that the total energy is conserved following the laser energy deposition occurring during the first 200 fs. Initially all the laser energy is deposited into the energy of electrons and then, within ~ 20 ps, is transferred to the thermal energy of the atomic motion. The fast temperature increase leads to the buildup of the compressive pressure in the middle of the irradiated film (see Sec. V) and induces acoustic vibrations of the film. The vibrations gradually dissipate into heat, which is reflected in a gradual transfer of energy from E_a^c to E_a^{th}. This energy transfer does not lead to the increase of the thermal energy, E_a^{th}, since it is offset by the transfer of energy from E_a^{th} to E_m. The time dependence of the energy of melting, E_m, reflects the two-step character of the melting process. A fast melting of $\sim 80\%$ of the film that takes place from ~ 10 ps to ~ 25 ps is followed by a much slower melting of the remaining part of the film. A detailed analysis of the melting mechanisms is performed in the next section.

V. LASER MELTING AND DISINTEGRATION OF Ni FILMS

The initial discussion of the redistribution of the absorbed laser energy and the mechanisms of laser melting is given below for a simulation performed for a 50 nm free-standing Ni film irradiated with a 200 fs laser pulse at an absorbed fluence of 430 J/m^2. This fluence is chosen so that we have a complete melting of the film by the end of the simulation. The laser energy absorption by the conduction band electrons, fast electron heat conduction, and gradual energy transfer to the lattice vibrations due to the electron-phonon coupling are reflected in Fig. 1(b), where the evolution of the electronic and lattice temperatures at the front and rear surfaces of the film is shown. The laser energy absorption results in a sharp increase of the electronic temperature near the irradiated front surface. The fast temperature-dependent electron heat conduction leads to the redistribution of the deposited energy within the film as reflected by the rise of the electronic temperature near the rear surface of the film. The process of the energy redistribution within the electronic system is occurring simultaneously with a more gradual energy transfer to the lattice vibrations due to electron-phonon coupling. As can be seen from Figs. 1(b) and 3, most of the energy is transferred to the lattice within ~ 5 ps, whereas complete equilibration between the hot electrons and the lattice takes up to 20 ps. The energy transferred to the lattice splits into three parts in Fig. 3, the energy of the thermal motion of the atoms, the energy of melting, and the energy of the collective atomic motion associated with elastic vibrations of the film. The latter part is associated with the relaxation of the laser-induced pressure and decreases with increasing laser pulse duration (see later in this section) or decreasing strength of the electron-phonon coupling (see Sec. VI).
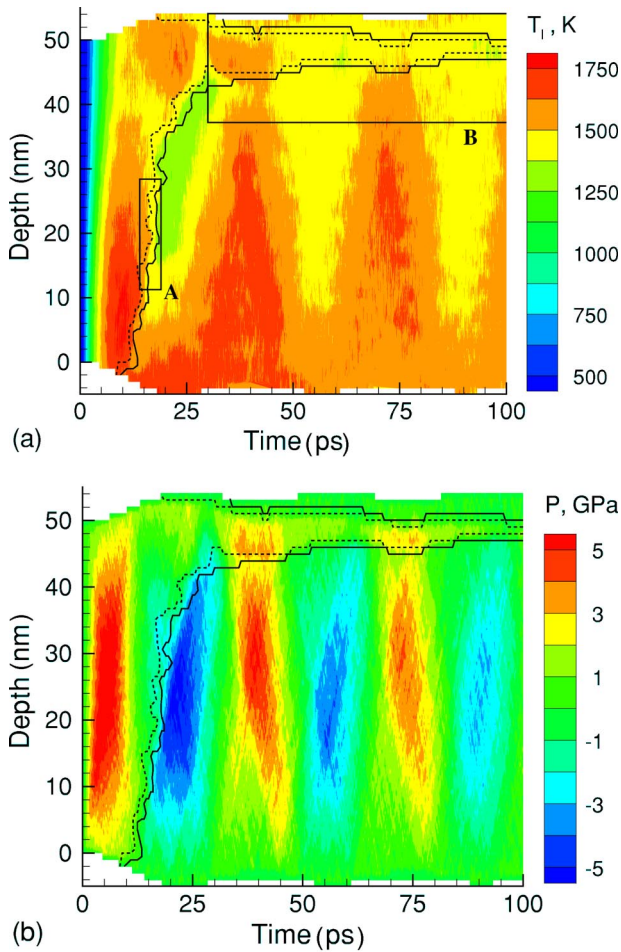
FIG. 4. (Color online) Contour plots of lattice temperature (a) and pressure (b) for simulation of laser melting of a 50 nm Ni film irradiated with a 200 fs laser pulse at an absorbed fluence of 430 J/m^2. Solid and dashed lines show the beginning and the end of the melting process. Rectangles *A* and *B* in (a) show the areas of the film and times for which snapshots are shown in Figs. 8 and 9, respectively. The laser pulse is directed along the *y* axes, from the bottom of the contour plots.

A. Analysis of the temperature evolution

The temporal and spatial evolution of the lattice temperature and pressure in the irradiated film is shown in the form of contour plots in Fig. 4. The motion of the front and back surfaces of the film corresponds to the initial thermal expansion of the film, followed by gradually dissipating oscillations. The complexity of the temperature plot, Fig. 4(a), reflects the interplay of several processes that are responsible for the lattice temperature evolution.

First, the energy transfer from hot electrons to the lattice leads to the initial temperature increase. A relatively small thermal diffusivity and strong electron-phonon coupling in Ni (as compared to other metals) leads to a rapid transfer of the absorbed energy to the lattice and the development of a temperature gradient within the 50 nm film during the first 10 ps of the simulation [Fig. 4(a)].

Second, the onset of melting leads to a decrease of the lattice temperature due to the transfer of a part of the thermal

energy to the latent heat of melting. A transient decrease of temperature due to the melting can be seen in Fig. 4(a), where the beginning and the end of the melting process are shown by the dashed and solid lines, respectively. The dashed line goes through the regions in the film where 10% of atoms have a "liquidlike" environment (as defined by the local order parameter, described in Appendix C), whereas the solid line connects the regions where 90% of atoms belong to the liquid phase.

Third, the elastic vibrations of the irradiated film caused by the relaxation of the laser-induced pressure have a significant effect on the temperature evolution in the film. Strong electron-phonon coupling in nickel leads to the steep rise of the lattice temperature during the first ~5 ps after the laser pulse [Figs. 1 and 4(a)]. The time of the lattice heating is shorter than the time needed for the film to expand in response to the corresponding thermoelastic stresses and, in the central part of the film, the heating takes place under the condition of inertial stress confinement.[62,69] The heating under the condition of stress confinement results in the buildup of high, up to 6 GPa, compressive pressure [Fig. 4(b)]. Relaxation of the compressive pressure leads to the expansion of the free-standing film with tensile stresses concentrating in the central part of the film. The following, gradually dissipating oscillations of the film can be described as propagation of two pressure waves trapped within the film that change their signs from compressive to tensile and vice versa at each reflection at the free surfaces. The dissipation of the oscillations is reflected in the gradual energy transfer from the energy of the collective atomic motion, E_a^c, to the energy of the thermal motion of the atoms, E_a^{th}, as can be seen from Fig. 3. The energy of the film oscillations decreases from ~15% of the total energy deposited by the laser pulse at 15 ps down to less than 10% by the time of 150 ps. A direct correlation between the pressure and temperature variations in the film is apparent from comparison of Figs. 4(a) and 4(b). Compression leads to the temperature increase whereas expansion corresponds to cooling. With the neglect of viscosity and dissipation of the energy of the elastic waves and considering the compression and expansion of the solid and liquid parts of the film as isentropic processes, the temperature variation with pressure can be estimated from classical thermodynamics,

$$(\partial T/\partial P)_S = VT\alpha/C_P . \tag{6}$$

In order to integrate this equation, we have to determine the pressure and temperature dependences of the heat capacity C_P, volume V, and the volume coefficient of thermal expansion α in both solid and liquid states. These dependences are calculated for the model EAM Ni material in a series of constant-pressure–constant-temperature simulations. The results of these simulations are shown in Figs. 5 and 6, where the temperature dependences of the volume and internal energy of the system are shown for different pressures. The volume plots (Fig. 5) allow us to calculate the volume coefficient of thermal expansion, $\alpha = (1/V) \times (\partial V/\partial T)_P$, for different temperatures and pressures. The internal energy plots (Fig. 6) provide us with the pressure
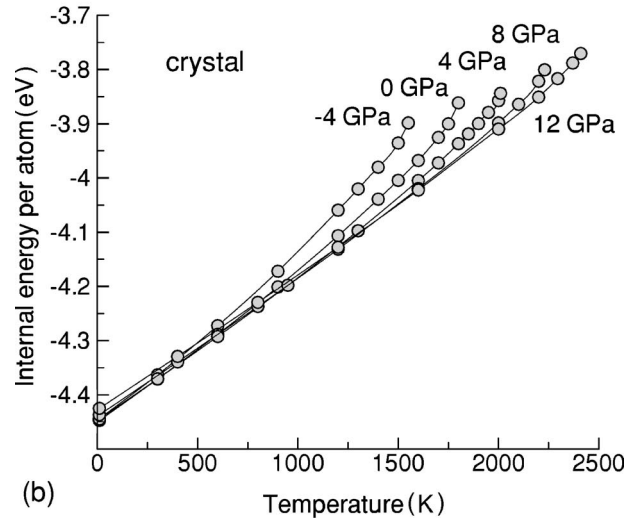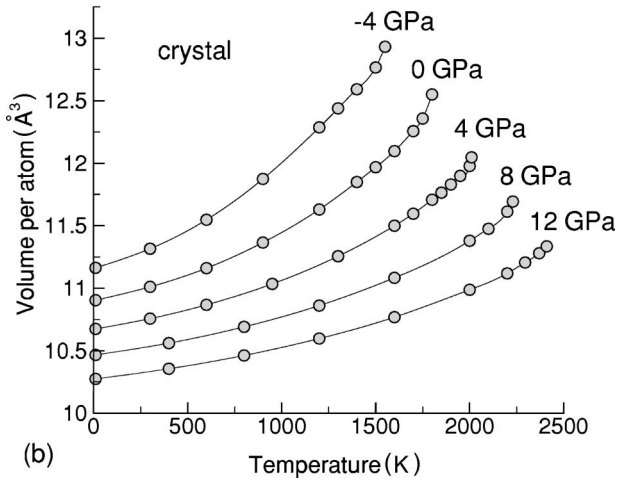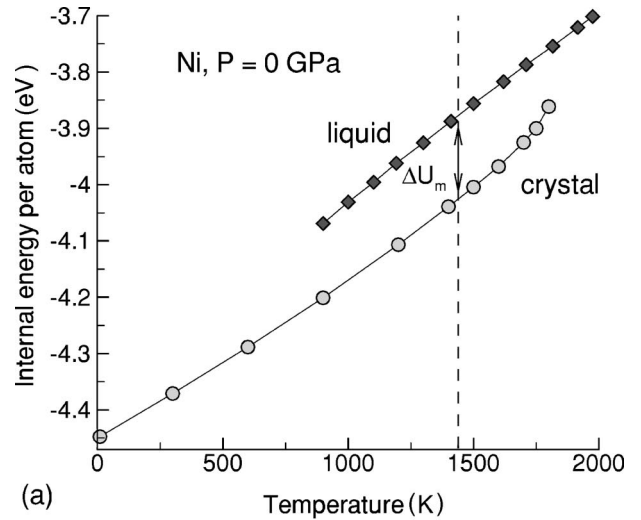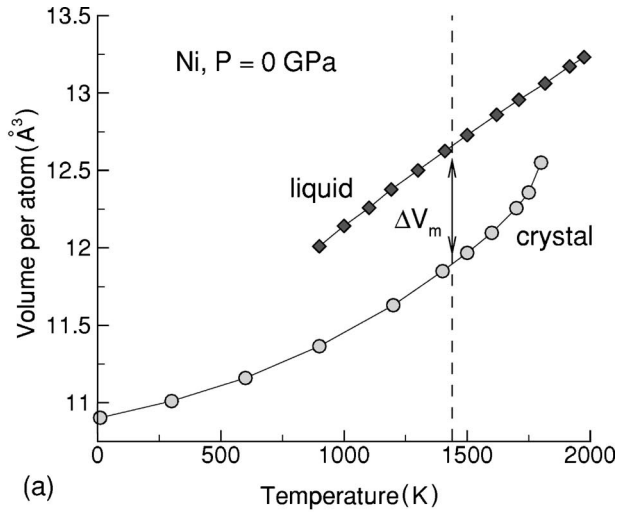
FIG. 5. The temperature dependence of the volume of the EAM Ni material. The results are shown for zero pressure for both solid and liquid phases in (a) and for several different pressures for the solid phase in (b). The dependences are used to calculate the volume coefficient of thermal expansion at different temperatures and pressures, $\alpha = (1/V)(\partial V/\partial T)_P$, and the volume change of melting, V_m, as indicated in (a). The vertical dashed line in (a) shows the equilibrium melting temperature of the EAM Ni at zero pressure.

and temperature dependence of the heat capacity, $C_P = (\partial H/\partial T)_P$. The knowledge of $C_P(T,P)$, $\alpha(T,P)$, and $V(T,P)$ allows us to integrate Eq. (6). The results of the integration are shown in Fig. 7, where the isentropes are shown for the crystal phase by dashed lines for several initial values of entropy. For a pressure variation from -5 to 5 GPa, observed in Fig. 4(b), the range of the temperature variation of ~ 200 K is predicted for the isentropic expansion/compression for both crystal (Fig. 7) and liquid (not shown) phases, in agreement with the temperature variation observed in Fig. 4(a).

The analysis performed above indicates that the complex temperature evolution in the irradiated film is defined by the interplay of the fast energy transfer from the excited electrons to the lattice vibrations, transfer of a part of the lattice

FIG. 6. The temperature dependence of the internal energy of the EAM Ni material. The results are shown for zero pressure for both solid and liquid phases in (a) and for several different pressures for the solid phase in (b). The dependences are used to calculate the heat capacity at different temperatures and pressures, $C_P = (\partial H/\partial T)_P$, as well as the latent heat of melting, $\Delta H_m = \Delta U_m + P\Delta V_m$, and the entropy change of melting, $\Delta S_m = \Delta H_m/T_m$. The vertical dashed line in (a) shows the equilibrium melting temperature of the EAM Ni at zero pressure.

thermal energy to the latent heat of melting, and the temperature variations related to the relaxation of the laser-induced pressure. The temperature and pressure evolution, in turn, defines the kinetics and the mechanisms of laser melting discussed in the next section.

B. Mechanisms of laser melting

Turning to the analysis of the mechanisms of laser melting, we can see from the dashed and solid lines separating the liquid- and solid-state regions in the contour plots shown in Fig. 4 that the melting process occurs in two steps. An ultrafast melting of $\sim 80\%$ of the film occurring within ~ 15
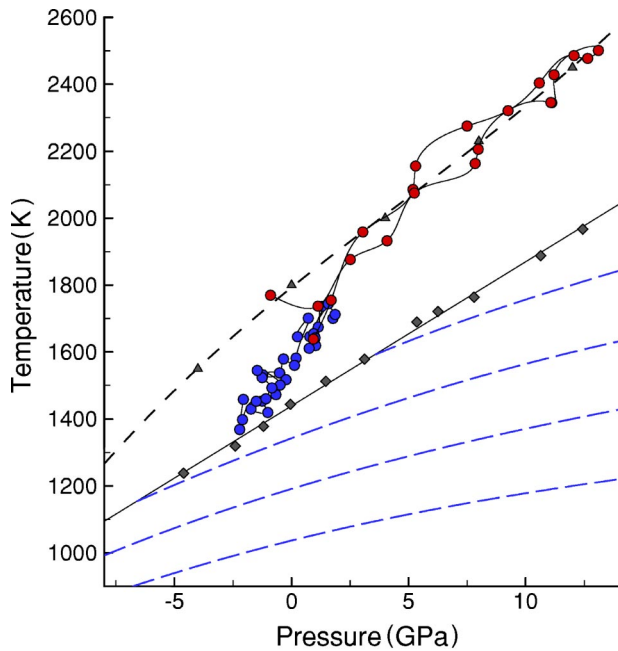
FIG. 7. (Color online) Conditions of equilibrium and nonequilibrium melting observed in simulations performed for the EAM Ni material. Black diamonds correspond to the conditions obtained in liquid-crystal coexistence simulations. Solid line shows the melting curve calculated from the Clapeyron equation. The four lower dashed lines are isentropes plotted for the crystal phase for four different values of entropy. Black triangles connected by the black dashed line correspond to the maximum overheating of the crystal observed in simulations performed with three-dimensional periodic boundary conditions. Blue and red circles correspond to the conditions leading to the onset of homogeneous melting in the simulations of laser irradiation of 50 nm Ni films at absorbed fluences of 430 J/m^2 and 1117 J/m^2, respectively. The conditions for the onset of homogeneous melting are realized along the dashed lines in Figs. 4 and 10 for the whole depth of the film in the simulation performed at 1117 J/m^2 and up to the depth of 35 nm in the simulation performed at 430 J/m^2. The circles are connected by lines in the order of increasing depth under the surface.
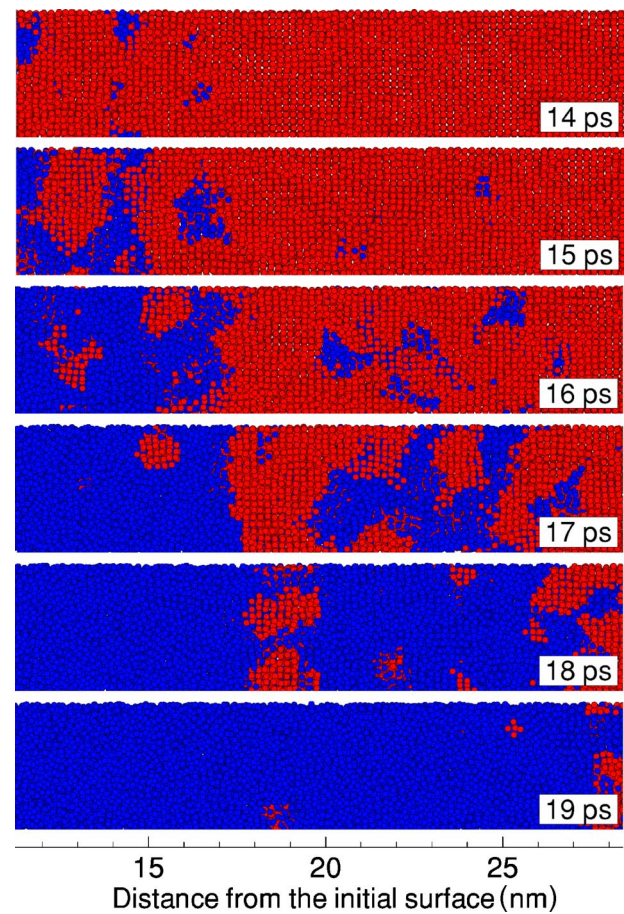

FIG. 8. (Color online) Snapshots from simulation of a 50 nm Ni film irradiated with a 200 fs laser pulse at an absorbed fluence of 430 J/m^2. Snapshots are taken at times and locations marked by rectangle A in Fig. 4(a). Atoms are colored according to the local order parameter—red atoms have local crystalline surroundings, blue atoms belong to the liquid phase. In these and other snapshots the atomic positions are averaged over 100 MD integration time steps (0.25 ps) in order to reduce the effect of thermal oscillations of atoms.

ps is followed by a much slower melting of the remaining crystalline region near the back surface of the film that takes more than 100 ps. The irradiated side of the film starts to melt $\sim$10 ps after the laser pulse, when the temperature reaches $\sim$1650 K, significantly above the equilibrium melting temperature of 1439 K, determined for the EAM Ni from a liquid-crystal coexistence simulation at zero pressure. During the following 15 ps a big part of the film melts and only a small layer near the back surface remains in a crystalline form. Although, at first sight, the melting seems to proceed by propagation of a melting front from the irradiated surface, a closer look at a series of snapshots of the atomic-level structure of a region undergoing ultrafast melting (Fig. 8) reveals a more complex picture characteristic of homogeneous melting. Small liquid regions appear and grow ahead of the "melting front," leading to a very high apparent "melting front" propagation velocity of $\sim$4000 m/s.

From the temperature contour plot [Fig. 4(a)] we see that although the homogeneous melting starts near the irradiated surface at a temperature of $\sim$1650 K, it proceeds at significantly lower temperatures that, in the central part of the film, become as low as $\sim$1300 K. This observation can be explained based on the pressure dependence of the equilibrium melting temperature. A series of liquid-crystal coexistence MD simulations has been performed at different pressures to determine the equilibrium melting temperature.[70] In these simulations a system of coexisting liquid and solid phases is allowed to evolve toward the equilibrium state while the energy of the system is conserved. If the temperature of the system is initially above the equilibrium melting temperature, part of the solid phase melts, consuming the latent heat of melting and reducing the temperature. If the initial temperature is lower than the equilibrium melting temperature, crystallization of a part of the system leads to the temperature evolution toward the equilibrium melting temperature from below. Simulation results, shown by diamonds in Fig. 7, predict a nearly linear dependence of the melting temperature on pressure. This prediction is in good agreement with

calculations based on the Clapeyron equation, $[dT/dP]_m \approx \Delta V_m / \Delta S_m$, where the volume change and entropy of melting, ΔV_m and ΔS_m, are determined from the temperature dependences of the volume and internal energy calculated as shown in Figs. 5(a) and 6(a), respectively. For the model EAM Ni material, the values of volume change and entropy of melting at zero pressure are found to be $\Delta V_m = 0.46$ cm^3/mol and $\Delta S_m = \Delta H_m / T_m = 10.06$ J/K mol, comparable to the experimental values for Ni, $\Delta V_m^{\text{expt}} = 0.32$ cm^3/mol and $\Delta S_m^{\text{expt}} = 9.94$ J/K mol.[71] In simulations we find that both ΔV_m and ΔS_m decrease with increasing pressure, leading to a weak nonmonotonous pressure dependence of the slope of the coexistence line with an average value of $[dT/dP]_m \approx 45$ K/GPa.

The temperature and pressure conditions leading to the onset of the ultrafast homogeneous laser melting are shown in Fig. 7 by blue circles. The conditions for the onset of homogeneous melting are calculated along the dashed line in Fig. 4 for the depth under the irradiated surface up to 35 nm. The circles are connected by a line in the order of increasing depth under the surface. At all pressures, the homogeneous melting starts under conditions of overheating above the liquid-crystal coexistence line. The overheating required for initiation of the homogeneous melting in this simulation is found to range from less than $1.05T_m$ to $1.18T_m$. These values of overheating are significantly lower then the highest temperature at which no homogeneous melting is observed in constant-pressure simulations performed with three-dimensional periodic boundary conditions. A series of such simulations has been performed for different pressures, and the observed temperatures required to melt the system, $(1.21-1.25)T_m$, are shown by triangles connected by a dashed line in Fig. 7. The temperatures at which melting takes place in a system with no external boundaries and internal defects correspond to the limit of thermal stability of the crystal lattice[8] and can be considered as the maximum possible overheating achievable in a system. The maximum overheating of $\sim 1.25T_m$ is observed at pressures from 0 to 10 GPa, whereas a gradual decrease of the overheating down to 1.21 GPa at -5 GPa is observed for negative pressures. The reasons for the discrepancy between the maximum overheating and the one required for the initiation of homogeneous melting under laser irradiation conditions are discussed in Sec. VII.

A region near the back surface of the irradiated film is not affected by the ultrafast homogeneous melting discussed above, and a much slower conventional heterogeneous melting takes place. A thin crystalline layer with two well-defined crystal-liquid interfaces is observed in a snapshot taken at 30 ps after the laser pulse in Fig. 9. The subsequent snapshots show that two melting fronts are propagating from the back surface of the film and from the homogeneously melted part of the film, leading to a gradual decrease of the size of the crystalline region and complete vanishing of the crystalline layer by the time of ~ 115 ps after the laser pulse. The heterogeneous melting is also affected by the pressure variations. The decrease in the thickness of the crystalline region typically coincides with the expansion of the region. This is related to the steeper slope of the coexistence line as com-
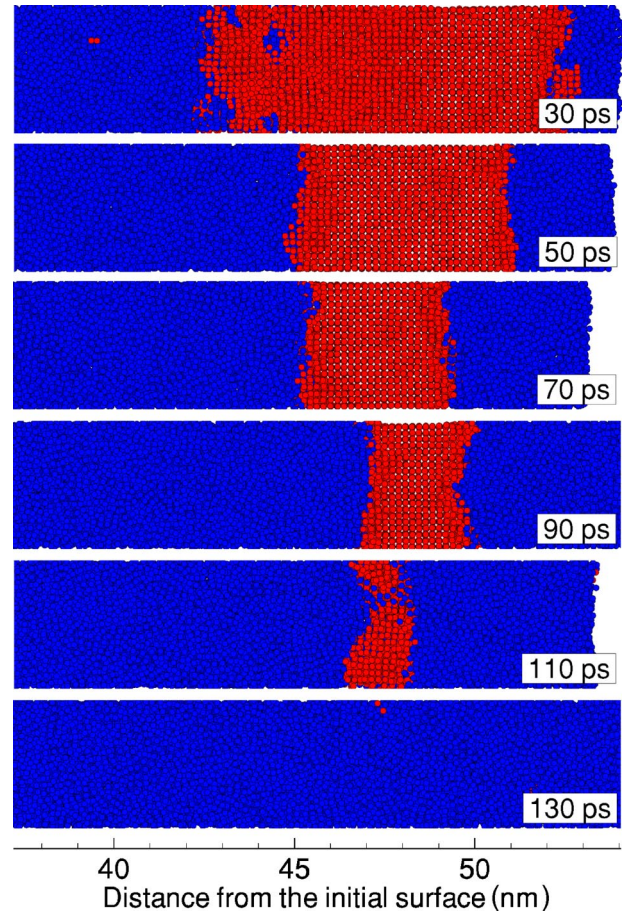

FIG. 9. (Color online) Snapshots from simulation of a 50 nm Ni film irradiated with a 200 fs laser pulse at an absorbed fluence of 430 J/m^2. Snapshots are taken at times and locations marked by rectangle B in Fig. 4(a). Atoms are colored according to the local order parameter—red atoms have local crystalline surroundings, blue atoms belong to the liquid phase.

pared to isentropes, $[dT/dP]_m > [dT/dP]_s$ (Fig. 7). Therefore, an adiabatic expansion of a region of the liquid-crystal coexistence facilitates melting and induces the advancement of the melting front.

C. Melting and disintegration at higher laser fluences

An increase of the laser fluence leads to a faster homogeneous melting of the entire film, eliminating the possibility for a slower heterogeneous melting by liquid-crystal interface propagation. Temperature and pressure evolution in a simulation performed with the same pulse duration as in the simulation discussed above, 200 fs, but with more than twice higher laser fluence of 1117 J/m^2 are shown in Fig. 10. From the dashed and solid lines that mark the beginning and the end of the melting process we see that the melting starts near the front surface at ~ 4 ps after the laser pulse and is over at ~ 11 ps. The visual analysis of the snapshots from the simulation (Fig. 11) suggests that homogeneous melting proceeds by nucleation of more numerous liquid regions that are smaller in size as compared to the lower fluence simulation (Fig. 8). The growth and coalescence of the liquid regions is
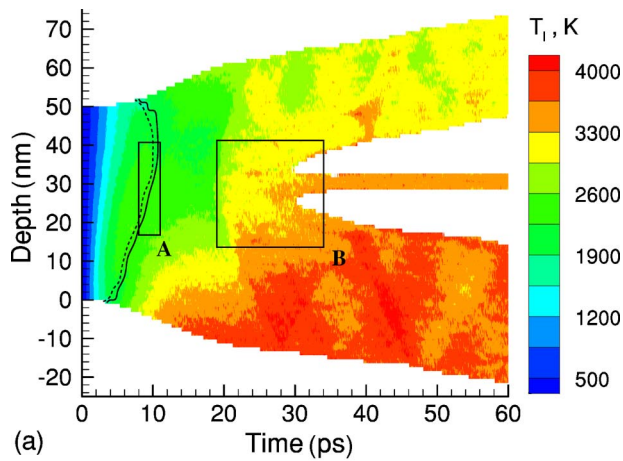
(a)
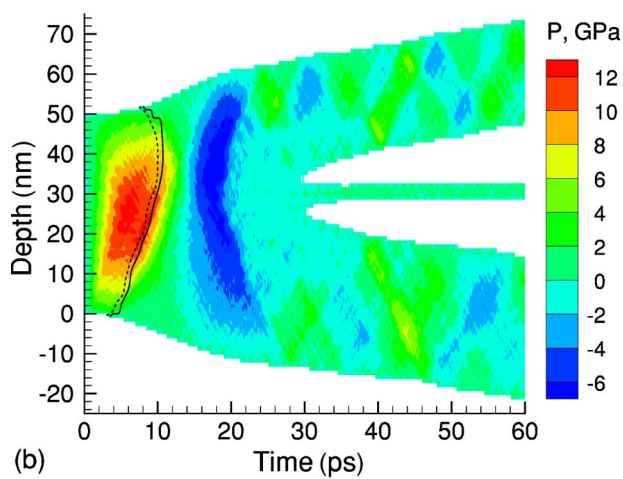
(b)

FIG. 10. (Color online) Contour plots of lattice temperature (a) and pressure (b) for simulation of laser melting of a 50 nm Ni film irradiated with a 200 fs laser pulse at an absorbed fluence of 1117 J/m². Solid and dashed lines show the beginning and the end of the melting process. Rectangles *A* and *B* in (a) show the areas of the film and times for which snapshots are shown in Figs. 11 and 12, respectively. The laser pulse is directed along the *y* axes, from the bottom of the contour plots.

also faster in simulations performed at higher fluences and it takes only ∼3 ps for a region shown in Fig. 11 to melt.

From the pressure plot in Fig. 10(b) we see that in the middle of the film the melting takes place at high compressive pressure. The pressure-temperature conditions for the onset of the homogeneous melting in this simulation are shown by red circles in Fig. 7. The circles are located in the region of compressive pressure and many of them are close or even above the dashed line, which shows the maximum possible overheating achievable in a system. These can be explained by the fact that at the time of melting the rate of the energy transfer from the hot electrons to the thermal motion of the atoms is still very high and the temperature calculated along the dashed line in Fig. 10 comes out higher than the one that is actually needed to initiate homogeneous melting.

The compressive pressure that builds up in the central part of the film due to the conditions of the stress confinement
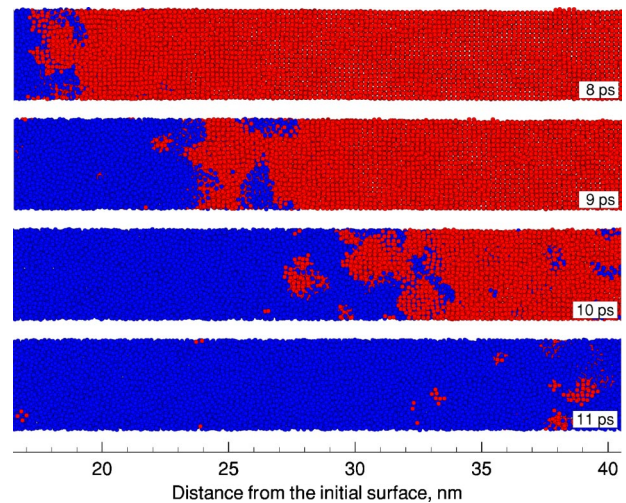

FIG. 11. (Color online) Snapshots from simulation of a 50 nm Ni film irradiated with a 200 fs laser pulse at an absorbed fluence of 1117 J/m². Snapshots are taken at times and locations marked by rectangle *A* in Fig. 10(a). Atoms are colored according to the local order parameter—red atoms have local crystalline surroundings, blue atoms belong to the liquid phase.

reaches its maximum of ∼12 GPa at ∼5 ps [Fig. 10(b)]. The maximum pressure is twice higher then the one observed in the simulation performed at a lower fluence of 430 J/m² [Fig. 4(b)]. In both simulations the relaxation of the compressive pressure leads to the expansion of the film and generation of the tensile stresses. In the case of the higher fluence, however, the tensile stresses are sufficient to cause disintegration of the film into two large pieces and one small piece moving apart from each other, as indicated by the two white gaps that develop in the contour plots shown in Fig. 10 after ∼30 ps. The disintegration interrupts the electronic heat conduction among the pieces of the film and the final temperatures of the front and the back pieces of the film are different by more than 500 K. One more consequence of the disintegration process is a strong asymmetry between the maximum compressive and tensile pressure observed in Fig. 10(b). Apparently, the dynamic strength of liquid Ni does not exceed 6 GPa and higher tensile stresses cannot be supported, leading to the void nucleation.

The atomic-level picture of the disintegration process is shown in Fig. 12. A number of voids appear in the central part of the film at ∼18 ps, the time when the tensile stresses reach their maximum values [Fig. 10(b)]. Some of the voids collapse, others grow, coalesce, and eventually lead to the disintegration of the film. Note that there are no gas-phase atoms observed inside the growing voids, indicating that the process of void nucleation and growth is not related to boiling but has a mechanical nature. Photomechanical processes caused by the relaxation of the laser-induced pressure and leading to disintegration of finite-size absorbers or damage/spallation of a surface region of an irradiated bulk target have been observed in experiments[69] as well as in MD simulations.[62,72,73]

D. The effect of pulse duration on melting mechanisms

The character of the melting and disintegration processes in irradiated films is in a big part defined by the rate of the
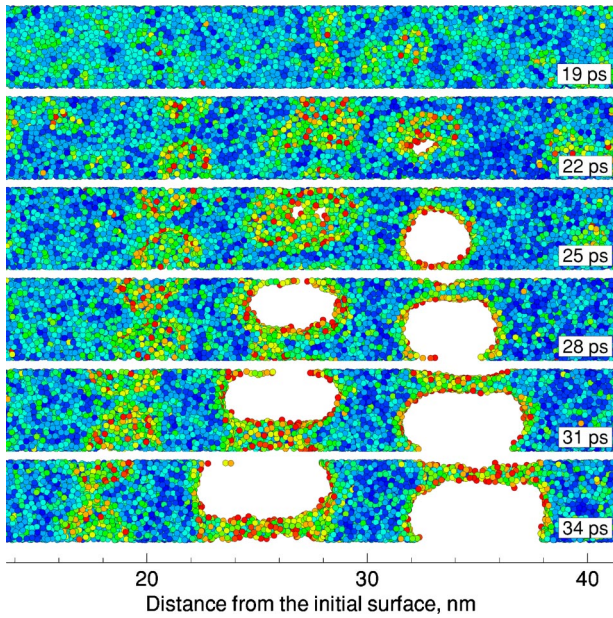
FIG. 12. (Color online) Snapshots from simulation of a 50 nm Ni film irradiated with a 200 fs laser pulse at an absorbed fluence of 1117 J/m^2. Snapshots are taken at times and locations marked by rectangle B in Fig. 10(a). Atoms are colored according to their potential energy (red color corresponds to a high potential energy of -2.5 eV, blue color corresponds to a low energy of -4 eV; the cohesive energy of the EAM Ni fcc crystal is 4.45 eV).

laser energy deposition into the thermal energy of atomic motion. The rate of lattice heating in short-pulse laser irradiation is defined by two factors, the strength of the electron-phonon coupling and the laser pulse duration. A comparison of the results obtained for Ni with the ones presented in the next section for Au allows us to discuss the role of the strength of the electron-phonon coupling, whereas the role of the pulse duration is investigated below in a series of simulations performed for Ni films.

The temperature contour plots are shown in Fig. 13 for simulations performed for the same laser fluence of 430 J/m^2 as in the simulation discussed in Secs. V A and V B, but with longer laser pulses of 50, 100, and 150 ps. In a clear contrast with the simulation performed with a 200 fs laser pulse (Fig. 4) the relaxation of the laser-induced pressure does not play any significant role in the simulations performed with the longer pulses. The conditions for the stress confinement[62,69] are not satisfied in these simulations, there is no significant pressure buildup in the central part of the film, and the film undergoes a gradual expansion rather than elastic oscillations observed in Fig. 4. Accordingly, the picture of the temperature evolution is less complex and is mainly defined by only two factors, the energy transfer from the excited electrons to the thermal energy of atomic motion and the transfer of a part of the lattice thermal energy to the latent heat of melting. The latter is reflected in a temporal temperature decrease right after the melting curves in Fig. 13.

In all of the three simulations, both homogeneous and heterogeneous melting mechanisms have been identified. The regions of the film where homogeneous nucleation of the liquid phase is observed are marked in Fig. 13 by dashed
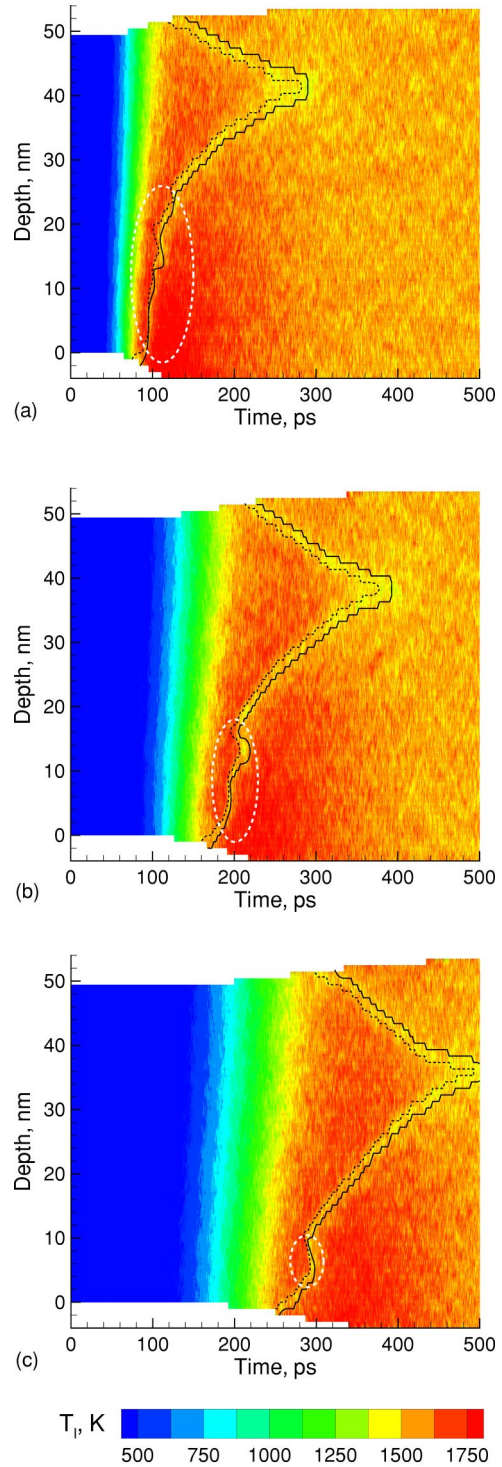

FIG. 13. (Color online) Contour plots of lattice temperature for simulations of a 50 nm Ni film irradiated by laser pulses with three different pulse durations, (a) 50 ps, (b) 100 ps, and (c) 150 ps. All simulations are performed at an absorbed fluence of 430 J/m^2. Solid and dashed lines show the beginning and the end of the melting process. The laser pulse is directed along the y axes, from the bottom of the contour plots. The regions where homogeneous nucleation of the liquid phase is observed are marked by the dashed ovals.
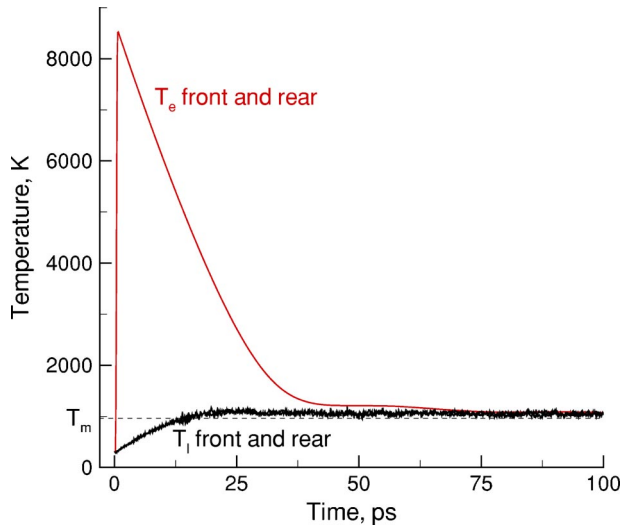
FIG. 14. (Color online) Time dependence of electron and lattice temperatures at the front and back surfaces of a 50 nm Au film irradiated with a 200 fs laser pulse at an absorbed fluence of 130 J/m^2. The dashed line shows the melting temperature of the EAM Au.

ovals. In simulations performed with 50 and 100 ps laser pulses, homogeneous nucleation is observed in relatively large regions near the front surface of the irradiated film. A much slower melting of the regions near the back surface of the films proceeds by propagation of two crystal-liquid interfaces from the back surface of the film and from the homogeneously melted part of the film. Velocity of the melting front propagation in heterogeneous melting depends on the overheating (see Sec. VII) and varies from ~180 m/s in the central parts of the films to ~60 m/s at the very end of the melting process. In the simulation performed with the 150 ps pulse, the melting starts at ~250 ps by a propagation of the liquid-crystal interface from the front surface. As the melting front propagates with velocity of ~130 m/s, a few liquid regions nucleate and grow at a depth of ~6–12 nm at ~290 ps, leading to an apparent jump in the melting front. No homogeneous nucleation of the liquid regions is observed in a simulation performed with a 200 ps laser pulse (not shown).

VI. LASER MELTING AND DISINTEGRATION OF Au FILMS

Simulations performed for gold films illustrate the effect of a weaker electron-phonon coupling on the melting process. This effect can be seen in Fig. 14, where the evolution of the electronic and lattice temperatures at the front and rear surfaces of the irradiated film is shown for a simulation performed at a laser fluence of 130 J/m^2 and pulse duration of 200 fs. Similarly to the simulation for Ni illustrated in Figs. 1, 3, 4, 8, and 9, this fluence is chosen to be close to the threshold for a complete melting of the film. A weak electron-phonon coupling and the ballistic energy transport by excited electrons[32,33] lead to a homogeneous heating of the 50 nm Au film. As a result, the electron and lattice temperature lines plotted in Fig. 14 for the front and back sur-
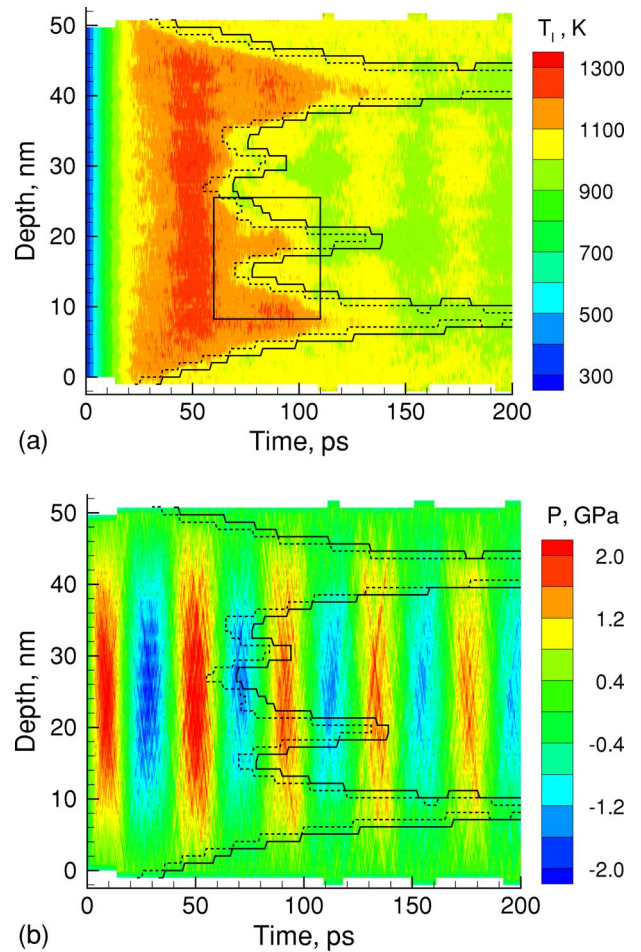

FIG. 15. (Color online) Contour plots of lattice temperature (a) and pressure (b) for simulation of laser melting of a 50 nm Au film irradiated with a 200 fs laser pulse at an absorbed fluence of 130 J/m^2. Solid and dashed lines show the beginning and the end of the melting process. The rectangle in (a) shows the area of the film and times for which snapshots are shown in Fig. 16. The laser pulse is directed along the y axes, from the bottom of the contour plots.

faces of the film are indistinguishable. The energy transfer to the lattice vibrations due to the electron-phonon coupling is slower in the Au film (Fig. 14) as compared to that of the Ni film [Fig. 1(b)]. Most of the energy is transferred to the lattice within ~15 ps, whereas complete equilibration between the hot electrons and the lattice takes up to 50 ps.

The lattice temperature evolution inside the film is shown in Fig. 15(a). The temperature increases throughout the film up to the time of ~50 ps. The pressure contour plot shows pressure oscillations similar to the ones observed in Fig. 4(b) for Ni. The pressure oscillations, however, are much weaker in Fig. 15(b) as compared to Fig. 4(b), and they have only a moderate effect on the temperature variations in Fig. 15(a). The reason for the weakness of the pressure oscillations observed in Au films is related to a relatively slow rate of the energy transfer from hot electrons to the thermal energy of the atomic motion. For laser pulses shorter than several tens of picoseconds, the rate of the lattice heating is limited by the weak electron-phonon coupling and only partial stress
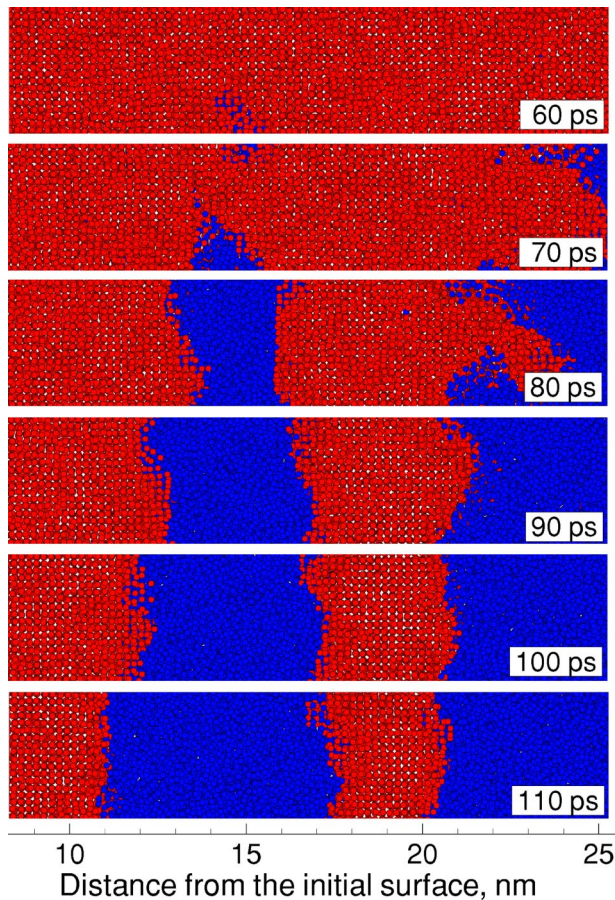
FIG. 16. (Color online) Snapshots from simulation of a 50 nm Au film irradiated with a 200 fs laser pulse at an absorbed fluence of 130 J/m². Snapshots are taken at times and locations marked by a rectangle in Fig. 15(a). Atoms are colored according to the local order parameter—red atoms have local crystalline surroundings, blue atoms belong to the liquid phase.
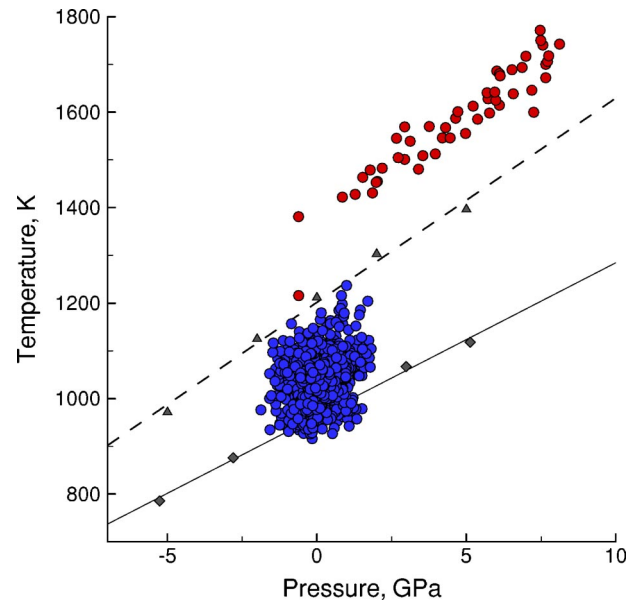

FIG. 17. (Color online) Conditions of equilibrium and nonequilibrium melting observed in simulations performed for the EAM Au material. Black diamonds correspond to the conditions obtained in liquid-crystal coexistence simulations. The solid line shows the melting curve calculated from the Clapeyron equation. Black triangles correspond to the maximum overheating of crystal observed in simulations performed with three-dimensional periodic boundary conditions, with the black dashed line being a linear fit to the data points. Blue and red circles correspond to the conditions leading to melting in simulations of laser irradiation of 50 nm Au films at absorbed fluences of 130 J/m² and 955 J/m², respectively. The conditions for the homogeneous nucleation of liquid regions (blue and red circles) as well as for the heterogenous growth of the liquid regions by melting front propagation (blue circles) are shown. The conditions correspond to the dashed lines in Figs. 15 and 18.

confinement can be achieved in 50 nm Au films even with very short laser pulses. The meaning of the partial stress confinement is apparent from Fig. 15—the period of the elastic vibrations of the film is ~43 ps and the film has an opportunity to expand while the thermal energy of the lattice is still increasing.

Analysis of the mechanism of melting in the simulation illustrated by Fig. 15 shows that the melting involves nucleation of three liquid regions inside the film and propagation of several melting fronts from the three liquid regions and the two free surfaces of the film. The atomic-level picture of the nucleation and growth of one of the liquid regions is shown in Fig. 16. By the time of 200 ps only two narrow crystalline regions still remain in the film (Fig. 15). Continuation of the simulation for a longer time shows that the crystalline region located closer to the front surface of the film disappears at ~250 ps, whereas the one located closer to the back surface remains indefinitely, as the temperature of the film settles down at the equilibrium melting temperature of the EAM Au, 963 K.

Using an analysis similar to the one discussed in detail for Ni in Secs. V A and V B, we determine the equilibrium liquid-crystal coexistence temperatures (solid line in Fig. 17) as well as the temperatures that correspond to the limit of crystal stability (dashed line in Fig. 17) for a range of pressures that are realized in the simulations. The temperature and pressure conditions leading to the onset of melting in the simulation discussed above are shown in Fig. 17 by blue circles. Unlike the blue circles in Fig. 7 that correspond to the conditions for homogeneous melting and do not include the part of the system where heterogeneous melting takes place, the blue dots in Fig. 17 are calculated along the whole dashed line shown in Fig. 15 and show the conditions leading to the homogeneous nucleation of the liquid regions along with the conditions at the liquid-crystal interfaces in the heterogeneous melting. Most of the dots in Fig. 17 are located between the two lines, with the highest density near the coexistence line. Therefore, melting is taking place predominantly under conditions of a moderate overheating. Some of the dots are located below the coexistence line, which can be explained by the temperature variations in the film due to the elastic vibrations (Fig. 15). As a result of the temperature variations the region of the liquid-crystal interface can undergo a transient moderate undercooling below the equilibrium melting temperature.

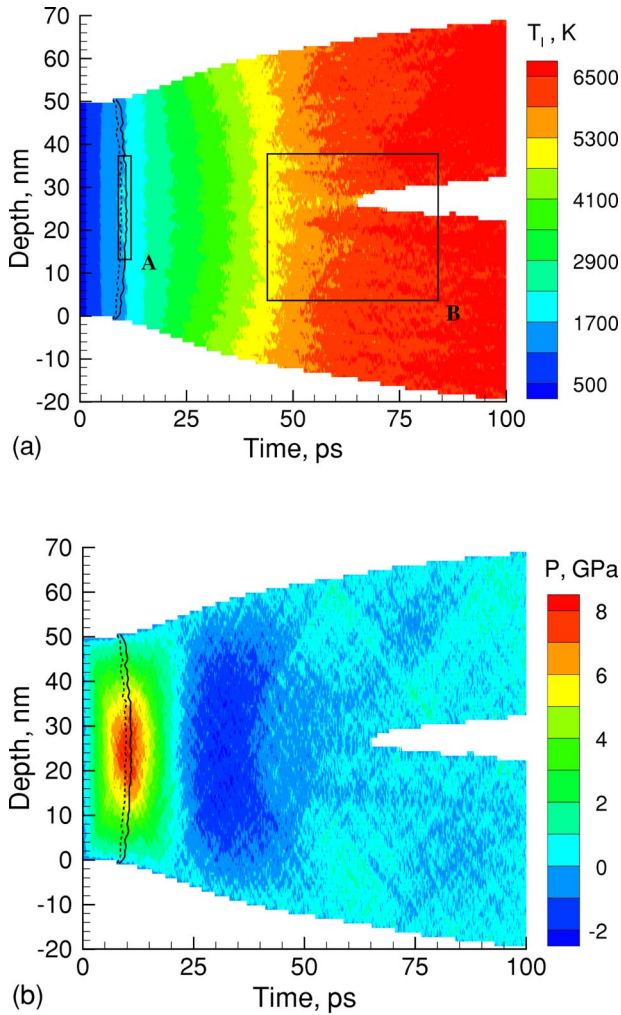The absence of strong stress confinement in the case of

(a)

(b)

FIG. 18. (Color online) Contour plots of lattice temperature (a) and pressure (b) for simulation of laser melting of a 50 nm Au film irradiated with a 200 fs laser pulse at an absorbed fluence of 955 J/m². Solid and dashed lines show the beginning and the end of the melting process. Rectangles *A* and *B* in (a) show the areas of the film and times for which snapshots are shown in Figs. 19 and 20, respectively. The laser pulse is directed along the *y* axes, from the bottom of the contour plots.

FIG. 19. (Color online) Snapshots from simulation of a 50 nm Au film irradiated with a 200 fs laser pulse at an absorbed fluence of 955 J/m². Snapshots are taken at times and locations marked by rectangle *A* in Fig. 18. Atoms are colored according to the local order parameter—red atoms have local crystalline surroundings, blue atoms belong to the liquid phase.

laser irradiation of 50 nm Au films makes it difficult to achieve the conditions for disintegration of the film. The pressure oscillations are not strong enough to induce photo-mechanical disintegration of the film up to the fluences at which the final temperature of the irradiated film significantly exceeds the boiling temperature of the material. The temperature and pressure evolution in a simulation performed at the lowest fluence at which disintegration of the film is observed, 955 J/m², is shown in Fig. 18. By the time of 10 ps the temperature exceeds the limit of crystal stability and the whole film melts within ~2 ps, as illustrated by the snapshots shown in Fig. 19. The liquid and crystal regions that can be identified during the phase transformation (snapshot at 10 ps) are not well defined and the melting process can be described as a simultaneous collapse of the crystal structure rather than homogeneous nucleation and growth of
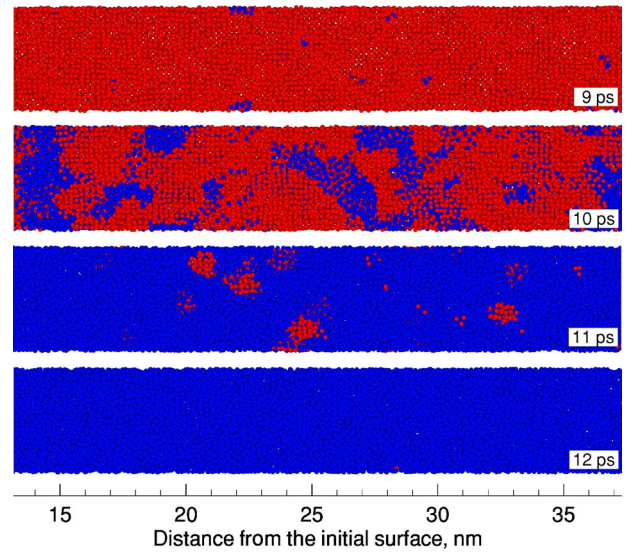
liquid regions. The conditions for this ultrafast phase transformation are shown by the red circles in Fig. 17. All the circles are located above the absolute limit of crystal stability. At these high overheatings the crystal collapses into a disordered state almost instantaneously, within a time comparable to 10–20 periods of atomic vibrations. This time needed for the transformation of the crystal structure to the disordered liquid state is, probably, the minimum time required for the thermal melting.[25]

After the melting at ~10 ps, the temperature continues to increase and at ~25 ps exceeds the boiling temperature of gold [Fig. 18(a)]. The compressive pressure that builds up in the central part of the film due to the conditions of the partial stress confinement reaches a maximum value of ~7 GPa at 10 ps and drives the expansion of the overheated film, leading to the generation of the tensile stresses at a time of 25–35 ps [Fig. 18(b)]. The maximum tensile stresses do not exceed −2 GPa and are much smaller then the maximum compressive stresses. The overheated material, however, cannot support any significant tension and responds to it by generation of several low-density regions and eventual disintegration (Fig. 20). The atomic-level picture of the disintegration process shown in Fig. 20 is different from the one of a Ni film illustrated in Fig. 12. The latter has the character of a mechanical disintegration of a liquid undergoing fast expansion and there are no gas-phase atoms inside the growing voids. In Fig. 20 material is overheated significantly above the boiling temperature and disintegration is accompanied by the onset of boiling and release of the gas-phase molecules.

VII. DISCUSSION AND SUMMARY

A comprehensive computational study of the fast non-equilibrium processes induced in 50 nm metal films by a
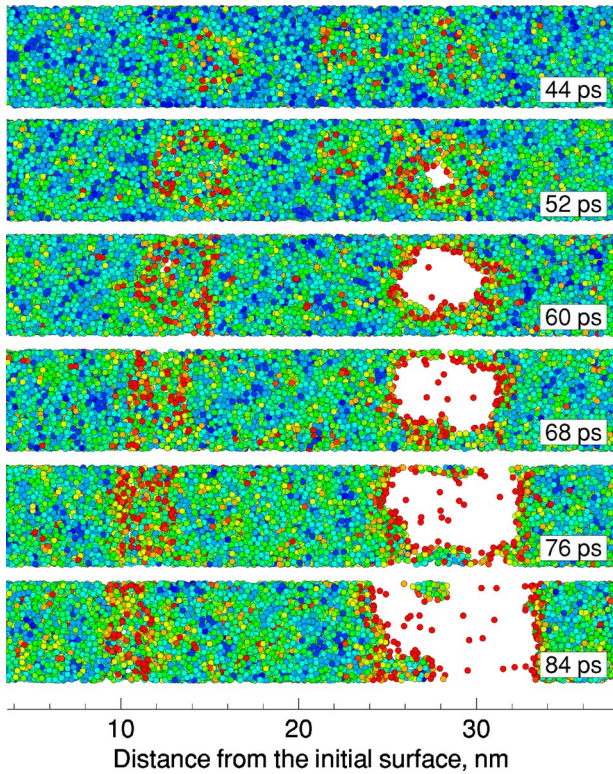
FIG. 20. (Color online) Snapshots from simulation of a 50 nm Au film irradiated with a 200 fs laser pulse at an absorbed fluence of 955 J/m^2. Snapshots are taken at times and locations marked by rectangle B in Fig. 18. Atoms are colored according to their potential energy (red color corresponds to high potential energy of -2 eV, blue color corresponds to low energy of -3.5 eV; the cohesive energy of the EAM Au fcc crystal is 3.93 eV).
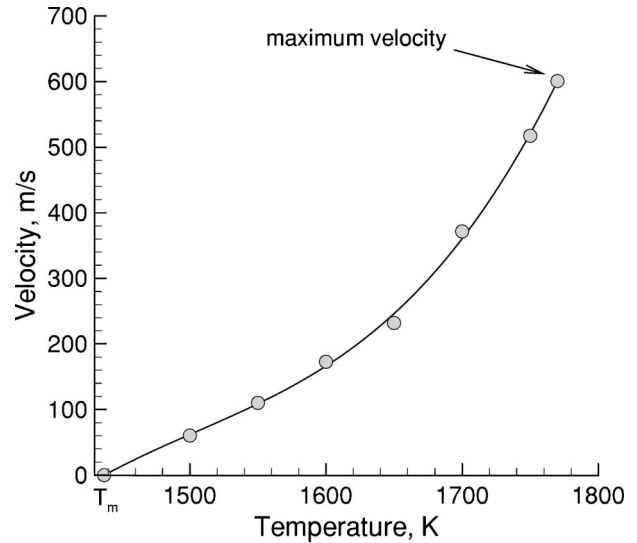

FIG. 21. The velocity of the melting front propagation in heterogeneous melting of an EAM Ni crystal as a function of temperature. The line is only a guide to the eye. The maximum velocity of the melting front propagation corresponds to the temperature above which an onset of homogeneous melting is observed.

short-pulse laser irradiation is performed for a range of irradiation conditions and two target materials, Ni and Au. Three distinct mechanisms of laser melting have been identified in the simulations, namely, homogeneous melting by nucleation and growth of liquid regions inside the crystal (e.g., Fig. 8), heterogeneous melting by propagation of liquid-crystal interfaces (melting fronts) from the external surfaces or homogeneously nucleated liquid regions (e.g., Figs. 9 and 16), and ultrafast, within $\sim$2 ps, collapse of the crystal structure overheated above a temperature that corresponds to the limit of crystal stability (e.g., Fig. 19). The process of ultrafast thermal melting is observed at high laser fluences, when the amount of the deposited laser energy significantly exceeds the one needed for a complete melting of the film.

At lower laser fluences, the relative contribution of the homogeneous and heterogeneous mechanisms of laser melting is defined by the rate of the lattice heating. One can expect that the contribution of the heterogeneous melting should increase as the heating time approaches the time needed for the melting fronts propagating from the external surfaces to pass through the irradiated film. The velocity of the melting front propagation as a function of the overheating above the equilibrium melting temperature has been measured for the EAM Ni material in a series of large-scale constant temperature simulations performed at zero pressure. The results, shown in Fig. 21, indicate that at small overheat-

ings, up to $\sim 1.15 T_m$, the velocity of the melting front propagation increases linearly with temperature. A faster increase of the melting front velocity is observed at higher temperatures and the maximum velocity of the melting front propagation is found to be $\sim$600 m/s at $T=1.23 T_m = 1770$ K. Above this temperature we observe homogeneous nucleation of liquid regions in the bulk of the crystal and the velocity of the melting front propagation cannot be defined. The value of the maximum velocity of the melting front propagation suggests that only the heterogeneous melting process can be expected to take place in a 50 nm Ni film irradiated by a laser pulse with duration of several tens of picoseconds or longer. In the laser melting simulations, however, we observe homogeneous nucleation of the liquid phase in increasingly smaller regions near the front surface of the film for laser pulse durations up to 150 ps (Fig. 13). This observation can be related to a significantly smaller overheating that is needed to induce homogeneous melting in laser melting simulations as compared to the constant-pressure–constant-temperature simulations with three-dimensional periodic boundary conditions. Indeed, in Fig. 7 all the blue dots corresponding to the conditions for homogeneous laser melting are located below the dashed line, corresponding to the conditions for homogeneous melting in the constant-pressure simulations. The reduced crystal stability in laser melting simulations can be explained by the strong pressure gradients transiently realized in the irradiated films and the associated complex stress conditions. Moreover, for a typical laser spot diameter of 10–100 μm the fast relaxation of the laser-induced pressure can only proceed in the direction normal to the surface. This uniaxial expansion and associated anisotropic lattice distortions can additionally reduce the lattice stability against the initiation of melting. The conditions of the lateral confinement in short-pulse laser irradiation are correctly reproduced by the periodic boundary

conditions in the directions parallel to the surfaces of the film. As a result, our simulations suggest that homogeneous melting can be induced at significantly lower overheating and a significantly larger range of irradiation parameters as compared to the predictions based on classical nucleation theory.[10]

The competition between the homogeneous and heterogeneous melting mechanisms is mainly defined by the laser pulse duration, as the electron-lattice equilibration times in metals are typically much shorter than the ones needed for heterogeneous melting. In contrast, the role of the laser-induced pressure in laser melting is defined not only by the pulse duration, but also by the strength of the electron-phonon coupling. The maximum values of the laser-induced pressure are related to the condition of the stress confinement that, for 50 nm films, is satisfied for the times of the lattice heating up to ~10 ps. In simulations performed for gold films the characteristic time of the energy transfer from the excited electrons to the lattice is longer, ~20 ps, as compared to nickel, ~5 ps. As a result, the laser-induced thermoelastic pressure is significantly weaker in the gold films and the effect of the pressure variations on laser melting mechanism is less pronounced even for the shortest, 200 fs, laser pulses used in the simulations. Similarly, the pressure variations are small and do not play any significant role in melting of Ni films irradiated with a laser pulse longer than 25 ps.

The process of relaxation of the laser-induced pressure in Ni films can lead to the generation of tensile stresses sufficiently strong to cause disintegration of the film. The process of disintegration proceeds by nucleation, growth, and coalescence of voids in the central region of an irradiated film, where the maximum tensile stresses are generated. The lower pressure that can be generated in Au films is not sufficient to induce photomechanical disintegration up to the fluences at which the disintegration process resembles that of an explosive boiling[46–48,62,63,74] of the film material assisted by moderate tensile stresses.

The strength of the electron-phonon coupling also defines whether a temperature gradient is established within a film of a given thickness. The strong electron-phonon coupling in Ni leads to the formation of a significant temperature gradient within the first 10 ps following irradiation by a short laser pulse (Figs. 1 and 4). In contrast, in simulations performed for gold films a weaker electron-phonon coupling and the ballistic energy transport by excited electrons lead to a homogeneous heating of a film of the same thickness (Figs. 14 and 15). The initial temperature distribution affects the kinetics of the laser melting process. In particular, the homogeneous melting of Ni films proceeds by nucleation and growth of liquid regions in an area quickly expanding from the front surface, resulting in an apparent "melting front" propagation from the front surface (Fig. 4). In contrast, in Au films nucleation of the liquid regions proceeds stochastically throughout the film (Fig. 15).

In summary, the results of the simulations present a comprehensive atomic-level picture of the competing homogeneous and heterogeneous mechanisms in laser melting. A combined atomistic-continuum computational model, used in the simulations, provides a detailed atomic-level description of fast nonequilibrium processes of laser melting and, at the same time, ensures an adequate description of the laser light absorption by the conduction band electrons, the energy transfer to the lattice due to the electron-phonon coupling, and the fast electron heat conduction. Both homogeneous and heterogeneous melting mechanisms are found to be responsible for laser melting of thin metal films, with relative contributions of these mechanisms defined by the laser fluence, pulse duration, and the strength of the electron-phonon coupling. The homogeneous nucleation of liquid regions inside the crystalline material is assisted by anisotropic lattice distortions and stress gradients induced by fast laser energy deposition. The lattice distortions and stress gradients reduce the overheating required for the initiation of homogeneous melting down to less then $T \approx 1.05 T_m$ and expand the range of pulse durations for which homogeneous melting is observed in 50 nm films up to ~150 ps. Under conditions of inertial stress confinement, realized in the case of short $\tau \leq 10$ ps laser pulses and strong electron-phonon coupling, the dynamics of the relaxation of the laser-induced pressure has a profound effect on the temperature distribution in the irradiated films as well as on both homogeneous and heterogeneous melting processes. At high laser fluences, significantly exceeding the threshold for melting, material can be quickly overheated above the limit of crystal stability, and an ultrafast, within ~2 ps, transition to the disordered state takes place simultaneously in the whole overheated region, eliminating the possibility for the intermediate liquid-crystal coexistence state.

APPENDIX A: COUPLING TERM FOR ENERGY EXCHANGE BETWEEN TTM AND MD

In the combined TTM-MD model the cells in the finite difference discretization are related to the corresponding volumes of the MD system and the local lattice temperature is defined from the average kinetic energy of thermal motion of atoms, K^T,

$$T_l = \frac{2K^T}{3k_B} = \sum_i m_i (\mathbf{v}_i^T)^2 / (3 k_B N^{\mathrm{cell}}), \tag{A1}$$

where the summation is performed over all the N^{cell} atoms in a given cell. In this definition, it is important to distinguish between the thermal velocities of the atoms, $\mathbf{v}_i^T$, and the velocities of the collective motion of atoms in a cell. For any atom, the thermal velocity is defined as $\mathbf{v}_i^T = \mathbf{v}_i - \mathbf{v}^c$, where $\mathbf{v}_i$ is the actual velocity of an atom i, and $\mathbf{v}^c$ is the velocity of the center of mass of a cell to which atom i belongs.

The energy exchange between the electrons and the lattice is described in the model by two coupling terms, $-G(T_e - T_l)$ in the diffusion equation for electrons [Eq. (3)], and $\xi m_i \mathbf{v}_i^T$ in the equation of motion of the atoms [Eq. (4)]. The

latter term serves the same purpose as does the coupling term $G(T_e - T_l)$ in the equation for the lattice temperature in TTM [Eq. (2)]. In order to define the coefficient ξ in the coupling term of Eq. (4) for each cell in the MD system, we have to relate the coefficient to the rate of the energy exchange and to make sure that this rate matches the one described by the coupling term $G(T_e - T_l)$ of the continuum equations.

Since the coupling term in Eq. (4) is affecting the thermal velocities of the atoms, let us consider the rate of the thermal kinetic energy change in a given cell of the MD system,

$$\frac{d}{dt}K^T = \frac{d}{dt}\sum_i \frac{m_i(\mathbf{v}_i^T)^2}{2} = \sum_i m_i\mathbf{v}_i^T\frac{d\mathbf{v}_i^T}{dt}$$

$$= \sum_i m_i\mathbf{v}_i^T\frac{d\mathbf{v}_i}{dt} - \sum_i m_i\mathbf{v}_i^T\frac{d\mathbf{v}^c}{dt}. \quad \text{(A2)}$$

Since the thermal velocities of atoms in a cell have random directions, the second term in the above equation can be neglected for sufficiently large cells. Therefore, using the equation of motion [Eq. (4)] and defining the rate of the energy deposition/extraction in a cell of a volume V_N according to the electron-phonon coupling term, we have

$$\frac{d}{dt}K^T = \sum_i m_i\mathbf{v}_i^T\frac{d\mathbf{v}_i}{dt} = \sum_i \mathbf{v}_i^T(\mathbf{F}_i + \xi m_i\mathbf{v}_i^T)$$

$$= \sum_i \mathbf{v}_i^T\mathbf{F}_i + \xi\sum_i m_i(\mathbf{v}_i^T)^2 = GV_N(T_e - T_l). \quad \text{(A3)}$$

Expressing the coefficient ξ from this equation we have

$$\xi = \frac{GV_N(T_e - T_l)}{\sum_i m_i(\mathbf{v}_i^T)^2} - \frac{\sum_i \mathbf{v}_i^T\mathbf{F}_i}{\sum_i m_i(\mathbf{v}_i^T)^2}. \quad \text{(A4)}$$

The second term in this equation is not related to the energy exchange with the electron subsystem of the model and is the result of the constraint on the thermal kinetic energy introduced by Eq. (A3). This constraint prevents any temperature fluctuations and limits the thermal kinetic energy variations to the controlled energy deposition due to the electron-phonon coupling. Actually, the second term in Eq. (A4) corresponds to a well-known Gaussian thermostat method for constant-temperature simulations.[75] In our model we do not want to prevent the natural temperature fluctuations in the system as well as temperature changes due to the phase transformations (e.g., melting leads to the transfer of a part of the kinetic energy to the latent heat of melting). Therefore we omit the second term in Eq. (A4) and leave only the term that is responsible for the controlled energy deposition due to the electron-phonon coupling:

$$\xi = \frac{GV_N(T_e - T_l)}{\sum_i m_i(\mathbf{v}_i^T)^2} = \frac{GV_N(T_e - T_l)}{2K^T}, \quad \text{(A5)}$$

where the lattice temperature is defined by Eq. (A1) and the coupling coefficient is recalculated at each MD integration time step for each cell defined by the finite difference discretization. As discussed in Sec. III, the time step of the finite difference integration of Eq. (4) is typically smaller then the

one used in the MD part of the model, $\Delta t_{MD} = n\Delta t_{FD}$, and the electron temperature can change during one MD time step. Therefore, the actual implementation of the algorithm involves averaging over a number of finite difference integration time steps that fits to one MD time step. The coefficient ξ is chosen so that the energy added to (or removed from) each cell of the MD system at each integration step, Δt_{MD}, would match the energy transferred between the electrons and the lattice during n steps of the finite difference integration,

$$\Delta E^{e\text{-ph}} = \sum_{k=1}^n \Delta t_{FD}GV_N(T_e^k - T_l), \quad \text{(A6)}$$

which leads to the following expression for ξ used in this work:

$$\xi = \frac{\frac{1}{\Delta t_{MD}}\Sigma_{k=1}^n \Delta t_{FD}GV_N(T_e^k - T_l)}{2K^T} = \frac{\frac{1}{n}\Sigma_{k=1}^n GV_N(T_e^k - T_l)}{2K^T}. \quad \text{(A7)}$$

Finally, we would like to emphasize the importance of making the distinction between the thermal and collective motion of atoms that has not been taken into account in earlier works.[54,65] Scaling the total velocities of atoms can introduce significant artifacts into the simulation results. As shown in Secs. V and VI, the relaxation of the laser-induced pressure in the irradiated films leads to large acoustic vibrations and, at high fluences, disintegration of the films. The energy of the collective motion of atoms associated with these processes can be comparable to the energy of the thermal motion of atoms, as can be seen in Fig. 3. Scaling the total velocities would artificially pump the energy into the energy of the acoustic vibrations, facilitate disintegration of the films, and accelerate any cluster that would form before the equilibrium between the local electron and lattice temperatures is reached. It is also essential to make the distinction between the thermal velocities and the velocities of collective motion of atoms in the definition of temperature [Eq. (A1)], and pressure, defined in MD simulations through the virial equation.

APPENDIX B: THERMAL CONDUCTIVITY OF Ni AND Au UNDER CONDITIONS OF ELECTRON-LATTICE NONEQUILIBRIUM

Due to the small heat capacity of the electrons in a metal, irradiation by a short, picosecond or femtosecond, laser pulse can lead to a large spike of the electron temperature within the absorption region of the irradiated target, as can be seen, for example, in Figs. 1 and 14. Therefore, the initial kinetics of the energy transport from the excited region deeper into the bulk of the target, described in TTM by the heat diffusion equation [Eqs. (1) or (3)], can be strongly affected by the character of the temperature dependence of the electron thermal conductivity. According to the Drude model,[76] the heat conductivity is proportional to the electron relaxation time τ_e, $K_e = (1/3)v_F^2 C_e \tau_e$, where v_F is the Fermi velocity. The
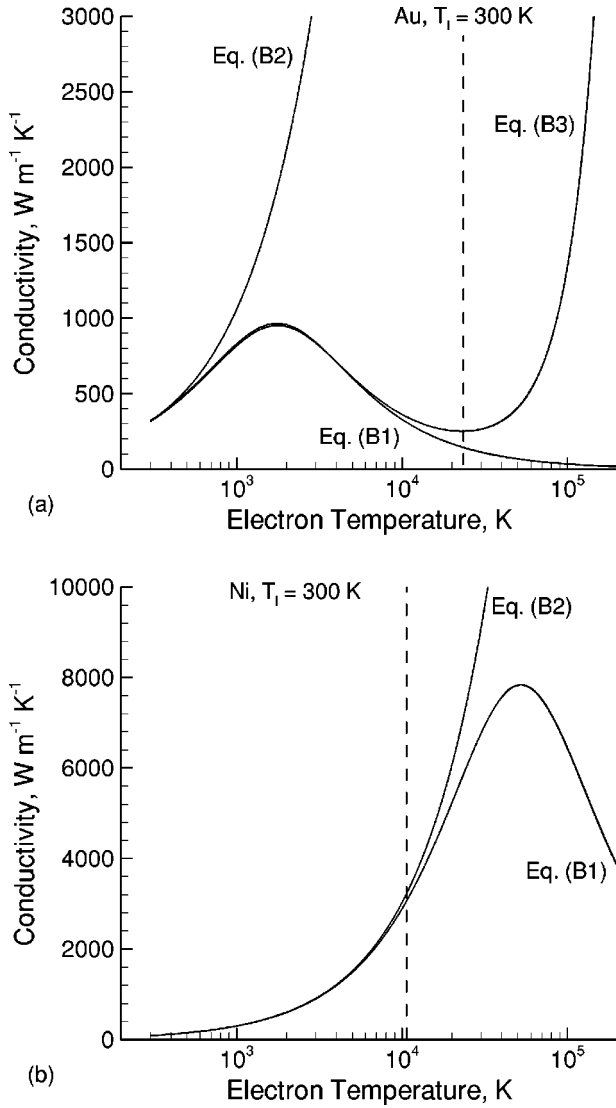
(a)

(b)

FIG. 22. Electron heat conductivity in Au and Ni described by different expressions [Eqs. (B1)–(B3)]. The lattice temperature is fixed at $T_l = 300$ K. Parameters used in the equations are $K_0 = 318$ W m^{-1} K^{-1} (Ref. 32), $A = 1.2 \times 10^7$ K^{-2} s^{-1}, $B = 1.23 \times 10^{11}$ K^{-1} s^{-1} (Ref. 77), $C = 353$ W m^{-1} K^{-1}, $b = 0.16$ (Ref. 78) for Au, and $K_0 = 91$ W m^{-1} K^{-1} (Ref. 32), $A = 1.4 \times 10^6$ K^{-2} s^{-1}, $B = 1.624 \times 10^{13}$ K^{-1} s^{-1} for Ni. The value of the constant A for Ni is calculated based on the model suggested in Ref. 80, whereas the value of the constant B for Ni is determined from fitting to Eq. (B2) in the low-temperature regime. The maximum electron temperatures realized in the simulations discussed in this work are marked by the vertical dashed lines.

electron relaxation time is defined by the electron-electron scattering time $\tau_{e\text{-}e}$ and electron-phonon scattering time $\tau_{e\text{-}ph}$, $1/\tau_e = 1/\tau_{e\text{-}e} + 1/\tau_{e\text{-}ph} = AT_e^2 + BT_l$, where A and B are constants.[77] Assuming a linear dependence of the electron heat capacity on the electron temperature, $C_e = \gamma T_e$, the expression for the thermal conductivity can be written as

$$K_e = \frac{1}{3} v_F^2 C_e \tau_e = \frac{1}{3} v_F^2 \frac{C_e}{AT_e^2 + BT_l} = \frac{1}{3} v_F^2 \frac{\gamma T_e}{AT_e^2 + BT_l}.$$
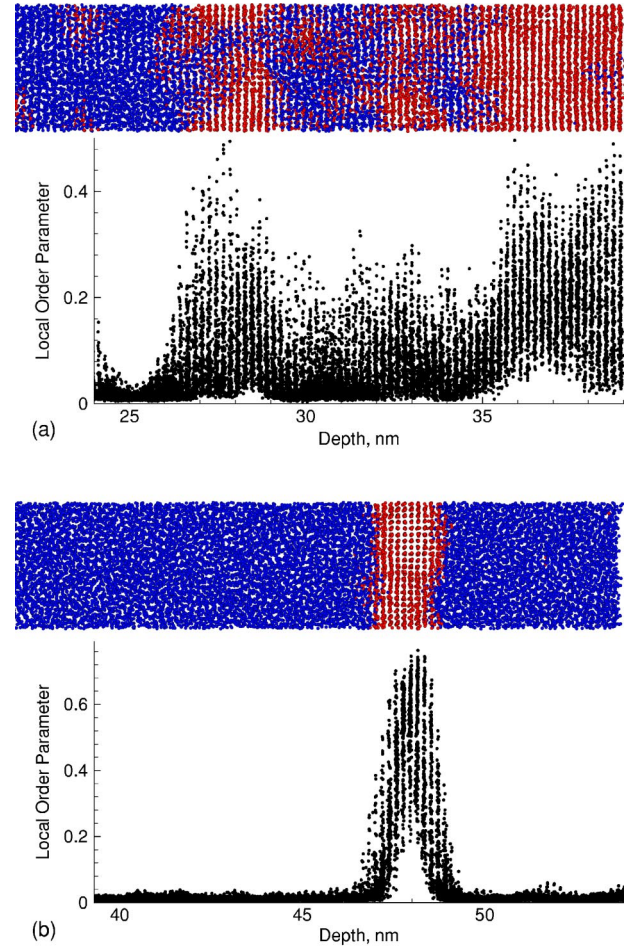
(B1)

FIG. 23. (Color online) Distribution of the local order parameter for two configurations encountered in the simulations of laser melting. A cutoff value of 0.04 is chosen for the local order parameter to distinguish between the crystalline and disordered atomic configurations.

At electron temperatures significantly below the Fermi temperature the contribution of the electron-phonon scattering dominates (e.g., $A = 1.2 \times 10^7$ K^{-2} s^{-1}, $B = 1.23 \times 10^{11}$ K^{-1} s^{-1} for gold[77] and $AT_e^2 = 1.08 \times 10^{12}$ s^{-1}, $BT_l = 3.69 \times 10^{13}$ s^{-1} at $T_e = T_l = 300$ K) and the contribution from the electron-electron scattering is often neglected, resulting in a linear dependence on the electron temperature,

$$K_e = K_0 \frac{T_e}{T_l}.$$

(B2)

This expression for the electron thermal conductivity is appropriate for low electron temperatures and is commonly used in calculations performed with TTM, e.g., Refs. 29, 31, 32, 35, 38, 39, and 54. It also results in a constant, temperature-independent thermal conductivity under conditions of thermal equilibrium between the electrons and the lattice. As the electron temperature approaches and exceeds the Fermi temperature ($T_F = 64\,200$ K for gold and $T_F = 136\,000$ K for nickel[76]) the electron gas becomes nondegenerate and the electronic heat conductivity starts to in-

crease with temperature, approaching the dependence $K_e \sim T_e^{5/2}$, characteristic for a low-density plasma. Equations (B1) and (B2) fail to predict the high-temperature behavior of the heat conductivity, and an alternative expression has been suggested and argued to be valid for a wide range of temperatures,[78]

$$K_e = C\vartheta_e \frac{(\vartheta_e^2 + 0.16)^{5/4}(\vartheta_e^2 + 0.44)}{(\vartheta_e^2 + 0.092)^{1/2}(\vartheta_e^2 + b\vartheta_1)}, \tag{B3}$$

where $\vartheta_e = T_e/T_F = k_B T_e/E_F$, $\vartheta_l = T_l/T_F = k_B T_l/E_F$, T_F and E_F are the Fermi temperature and energy, respectively, and C and b are parameters that can be determined from experimental data. For high electron temperatures, $\vartheta_e \gg 1$, Eq. (B3) reduces to the dependence characteristic for a low-density plasma, $K_e \sim T_e^{5/2}$, whereas in the low-temperature limit, $\vartheta_e \ll 1$, Eq. (B3) reduces to Eqs. (B1) and (B2).

The dependence of the electron heat conductivity from the electron temperature is shown in Fig. 22 for the metals investigated in this work, gold and nickel, and for a fixed lattice temperature of 300 K. A significantly lower Fermi temperature of gold as compared to nickel results in the onset of deviations among the predictions of Eqs. (B1)–(B3) at a lower temperature. The highest electron temperature in simulations performed for Ni films is 10 500 K and the approximation given by Eq. (B2) is adequate. For simulations performed for Au films, the maximum electron temperature is 23 300 K and the most general expression given by Eq. (B3) should be used. Therefore, in this work we use Eq. (B2) with $K_0 = 91$ W m^{-1} K^{-1} (Ref. 32) in simulations performed for Ni and Eq. (B3) with $C = 353$ W m^{-1} K^{-1}, $b = 0.16$ (Ref. 78), and $T_F = 64\,200$ K (Ref. 76) in simulations performed for Au.

APPENDIX C: LOCAL ORDER PARAMETER FOR IDENTIFICATION OF LIQUID AND CRYSTAL REGIONS

The identification of liquid and crystal regions in the atomic configurations produced in the simulations of ul-

trafast laser melting is often challenging due to the complex nature of the melting process and the absence of well-defined plane liquid-crystal interfaces (e.g., Figs. 8, 11, and 19). In this work a distinction between the original fcc structure and the liquid phase is made with the local order parameter defined as[70]

$$\Psi_i = \left| \frac{1}{6} \frac{1}{Z} \sum_{j=1}^{Z} \sum_{k=1}^{6} \exp(i\mathbf{q}_k \cdot \mathbf{r}_{ij}) \right|^2,$$

where the first summation with k is over a set of six vectors $\{\mathbf{q}_k\}$ chosen so that $\exp(i\mathbf{q}_k\mathbf{r}_{ij}) = 1$ for any vector $\mathbf{r}_{ij}$ connecting atom i with atom j in the first- or second-neighbor shell in a perfect fcc lattice, and the second summation with j is over all the atoms found within a cutoff distance r_{cut} from atom i. The cutoff distance r_{cut} is chosen so that the first two neighbor shells in a perfect fcc lattice are included. The choice of the six vectors $\{\mathbf{q}_k\}$ is not unique, and the following set of vectors was found to provide an optimum sensitivity of the method: $\mathbf{q}_1 = (4\pi/a_{fcc})(1,0,0)$, $\mathbf{q}_2 = (4\pi/a_{fcc}) \times (0,1,0)$, $\mathbf{q}_3 = (4\pi/a_{fcc})(0,0,1)$, $\mathbf{q}_4 = (4\pi/a_{fcc})(1,1,0)$, $\mathbf{q}_5 = (4\pi/a_{fcc})(0,1,1)$, $\mathbf{q}_6 = (4\pi/a_{fcc})(1,0,1)$, where a_{fcc} is the fcc lattice parameter.

In order to reduce the effect of the thermal atomic vibrations on the result of the structural analysis, the atomic positions used in the calculation of Ψ_i are averaged over 0.25 ps. Moreover, the local order parameter was by itself averaged over the neighboring atoms, as suggested in Ref. 70,

$$\bar{\Psi}_i = \frac{1}{Z+1}\left(\Psi_i + \sum_{j=1}^{Z} \Psi_j \right).$$

As shown in Fig. 23, the local order parameter defined above provides a quantitative measure of the "degree of crystallinity" of the local atomic configurations that agrees well with a visual analysis. The local order parameter changes from 0 to 1 with a value of $\bar{\Psi}_i = 0.04$ chosen in this work to distinguish between the liquid and crystal structures.

---

*E-mail address: lz2n@virginia.edu

 URL: http://www.faculty.virginia.edu/CompMat/

[1] D. Bäuerle, *Laser Processing and Chemistry* (Springer, Berlin, 2000).

[2] *Pulsed Laser Deposition of Thin Films*, edited by D. B. Chrisey and G. K. Hubler (Wiley-Interscience, New York, 1994).

[3] J. Jersch, F. Demming, J. Hildenhagen, and K. Dickmann, Opt. Laser Technol. **29**, 433 (1997).

[4] J. Wang, J. Li, S. Yip, D. Wolf, and S. Phillpot, Physica A **240**, 396 (1997).

[5] K. Lu and Y. Li, Phys. Rev. Lett. **80**, 4474 (1998).

[6] J. G. Dash, Rev. Mod. Phys. **71**, 1737 (1999).

[7] J. F. Van der Veen, Surf. Sci. **433–435**, 1 (1999).

[8] Z. H. Jin, P. Gambsch, K. Lu, and E. Ma, Phys. Rev. Lett. **87**, 055703 (2001).

[9] R. W. Cahn, Nature (London) **413**, 582 (2001).

[10] B. Rethfeld, K. Sokolowski-Tinten, D. von der Linde, and S. I. Anisimov, Phys. Rev. B **65**, 092103 (2002).

[11] P. R. Couchman and W. A. Jesser, Nature (London) **269**, 481 (1977).

[12] R. W. Cahn, Nature (London) **342**, 619 (1989).

[13] Z. H. Zhang and H. E. Elsayed-Ali, Surf. Sci. **405**, 271 (1998).

[14] D. P. Woodruff, *The Solid-Liquid Interface* (Cambridge University Press, Cambridge, 1973).

[15] S. Williamson, G. Mourou, and J. C. M. Li, Phys. Rev. Lett. **52**, 2364 (1984).

[16] J. W. Herman and H. E. Elsayed-Ali, Phys. Rev. Lett. **69**, 1228 (1992).

[17] K. Sokolowski-Tinten, J. Bialkowski, M. Boing, A. Cavalleri, and D. von der Linde, Phys. Rev. B **58**, R11 805 (1998).

[18] M. B. Agranat, S. I. Ashitkov, V. E. Fortov, A. V. Kirillin, A. V. Kostanovskii, S. I. Anisimov, and P. S. Kondratenko, Appl. Phys. A: Mater. Sci. Process. **69**, 637 (1999).

[19] V. Schmidt, W. Husinsky, and G. Betz, Phys. Rev. Lett. **85**, 3516 (2000).

[20] B. Lin and H. E. Elsayed-Ali, Surf. Sci. **498**, 275 (2002).

[21] K. Sokolowski-Tinten, C. Blome, J. Blums, A. Cavalleri, C. Dietrich, A. Tarasevich, I. Uschmann, E. Förster, M. Kammler, M. Horn-von-Hoegen, and D. von der Linde, Nature (London) **422**, 287 (2003).

[22] O. P. Uteza, E. G. Gamaly, A. V. Rode, M. Samoc, and B. Luther-Davies (unpublished).

[23] F. Spaepen and D. Turnbull, in *Laser-Solid Interactions and Laser Processing*, edited by S. D. Ferris, H. J. Leamy, and J. M. Poate, AIP Conf. Proc. No. 50 (AIP, New York, 1979), pp. 73–83.

[24] V. I. Motorin and S. L. Musher, Zh. Tekh. Fiz. **52**, 1200 (1982) [Sov. Phys. Tech. Phys. **27**, 726 (1982)].

[25] Observations of an even more rapid nonthermal melting occurring on a subpicosecond time scale have been reported for covalently bonded materials irradiated by intense femtosecond laser pulses [C. V. Shank, R. Yen, and C. Hirlimann, Phys. Rev. Lett. **51**, 900 (1983); P. Saeta, J.-K. Wang, Y. Siegal, N. Bloembergen, and E. Mazur, *ibid.* **67**, 1023 (1991); C. W. Siders, A. Cavalleri, K. Sokolowski-Tinten, Cs. Toth, T. Guo, M. Kammler, M. Horn von Hoegen, K. R. Wilson, D. von der Linde, and C. P. J. Barty, Science **286**, 1340 (1999); A. Rousse, C. Rischel, S. Fourmaux, I. Uschmann, S. Sebban, G. Grillon, Ph. Balcou, E. Forster, J. P. Geindre, P. Audebert, J. C. Gauthier, and D. Hulin, Nature (London) **410**, 65 (2001)]. The nonthermal character of the melting is apparent from the fact that it takes place faster than the time of several picoseconds needed for the carrier-lattice equilibration. Theoretical analysis suggests that such an ultrafast melting can be attributed to the dramatic weakening of the covalent bonding due to the laser excitation of a large number, more than $\sim 10\%$, of valence electron to the conduction band [P. Stampfli and K. H. Bennemann, Appl. Phys. A: Mater. Sci. Process. **60**, 191 (1995); P. L. Silvestrelli, A. Alavi, M. Parrinello, and D. Frenkel, Phys. Rev. Lett. **77**, 3149 (1996)]. Investigation of the mechanisms of the nonthermal melting is beyond the scope of the present study since it is focused on laser interaction with metals.

[26] M. I. Kaganov, I. M. Lifshitz, and L. V. Tanatarov, Zh. Eksp. Teor. Fiz. **31**, 232 (1956) [Sov. Phys. JETP **4**, 173 (1957)].

[27] S. I. Anisimov, B. L. Kapeliovich, and T. L. Perel'man, Zh. Eksp. Teor. Fiz. **66**, 776 (1974) [Sov. Phys. JETP **39**, 375 (1974)].

[28] G. L. Eesley, Phys. Rev. B **33**, 2144 (1986).

[29] A. N. Smith and P. M. Norris, Appl. Phys. Lett. **78**, 1240 (2001).

[30] J. L. Hostetler, A. N. Smith, and P. M. Norris, Int. J. Thermophys. **19**, 569 (1998).

[31] P. M. Norris, A. P. Caffrey, R. J. Stevens, J. M. Klopf, J. T. McLeskey, Jr., and A. N. Smith, Rev. Sci. Instrum. **74**, 400 (2003).

[32] J. Hohlfeld, S.-S. Wellershoff, J. Güdde, U. Conrad, V. Jähnke, and E. Matthias, Chem. Phys. **251**, 237 (2000).

[33] J. Hohlfeld, J. G. Müller, S.-S. Wellershoff, and E. Matthias, Appl. Phys. A: Mater. Sci. Process. **64**, 387 (1997).

[34] H. E. Elsayed-Ali, T. Juhasz, G. O. Smith, and W. E. Bron, Phys. Rev. B **43**, 4488 (1991).

[35] J. L. Hostetler, A. N. Smith, D. M. Czajkowsky, and P. M. Norris, Appl. Opt. **38**, 3614 (1999).

[36] J. H. Hodak, A. Henglein, and G. V. Hartland, J. Chem. Phys. **112**, 5942 (2000).

[37] N. Del Fatti and F. Vallée, C. R. Phys. **3**, 365 (2002).

[38] S.-S. Wellershoff, J. Hohlfeld, J. Güdde, and E. Matthias, Appl. Phys. A: Mater. Sci. Process. **69**, S99 (1999).

[39] P. J. Antaki, Int. J. Heat Mass Transfer **45**, 4063 (2002).

[40] V. Schmidt, W. Husinsky, and G. Betz, Appl. Surf. Sci. **197**, 145 (2002).

[41] T. Q. Qiu and C. L. Tien, J. Heat Transfer **115**, 842 (1993).

[42] J. K. Chen and J. E. Beraun, Numer. Heat Transfer, Part A **40**, 1 (2001).

[43] L. A. Falkovsky and E. G. Mishchenko, Zh. Eksp. Teor. Fiz. **115**, 149 (1999) [JETP **88**, 84 (1999)].

[44] J. K. Chen, J. E. Beraun, L. E. Grimes, and D. Y. Tzou, Int. J. Solids Struct. **39**, 3199 (2002).

[45] S. I. Kudryashov and V. I. Emel'yanov, Pis'ma Zh. Eksp. Teor. Fiz. **73**, 751 (2001) [JETP Lett. **73**, 666 (2001)].

[46] A. Miotello and R. Kelly, Appl. Phys. A: Mater. Sci. Process. **69**, S67 (1999).

[47] R. Kelly and A. Miotello, J. Appl. Phys. **87**, 3177 (2000).

[48] N. M. Bulgakova and A. V. Bulgakov, Appl. Phys. A: Mater. Sci. Process. **73**, 199 (2001).

[49] F. Vidal, T. W. Johnston, S. Laville, O. Barthélemy, M. Chaker, B. Le Drogoff, J. Margot, and M. Sabsabi, Phys. Rev. Lett. **86**, 2573 (2001).

[50] K. Sokolowski-Tinten, J. Bialkowski, A. Cavalleri, D. von der Linde, A. Oparin, J. Meyer-ter-Vehn, and S. I. Anisimov, Phys. Rev. Lett. **81**, 224 (1998).

[51] Z. H. Jin and K. Lu, Philos. Mag. Lett. **78**, 29 (1998).

[52] M. D. Kluge, J. R. Ray, and A. Rahman, J. Chem. Phys. **87**, 2336 (1987).

[53] F. F. Abraham and J. Q. Broughton, Phys. Rev. Lett. **56**, 734 (1986).

[54] H. Häkkinen and U. Landman, Phys. Rev. Lett. **71**, 1023 (1993).

[55] F. F. Abraham, D. E. Schreiber, M. R. Mruzik, and G. M. Pound, Phys. Rev. Lett. **36**, 261 (1976).

[56] J. A. Blink and W. G. Hoover, Phys. Rev. A **32**, 1027 (1985).

[57] Wm. T. Ashurst and B. L. Holian, Phys. Rev. E **59**, 6742 (1999).

[58] L. V. Zhigilei and B. J. Garrison, Mater. Res. Soc. Symp. Proc. **538**, 491 (1999).

[59] J. I. Etcheverry and M. Mesaros, Phys. Rev. B **60**, 9430 (1999).

[60] R. F. W. Herrmann, J. Gerlach, and E. E. B. Campbell, Appl. Phys. A: Mater. Sci. Process. **66**, 35 (1998).

[61] E. Ohmura, I. Fukumoto, and I. Miyamoto, Int. J. Jpn. Soc. Precis. Eng. **32**, 248 (1998).

[62] L. V. Zhigilei and B. J. Garrison, J. Appl. Phys. **88**, 1281 (2000).

[63] L. V. Zhigilei, Appl. Phys. A: Mater. Sci. Process. **76**, 339 (2003).

[64] M. W. Finnis, P. Agnew, and A. J. Foreman, Phys. Rev. B **44**, 567 (1991).

[65] C. Schäfer, H. M. Urbassek, and L. V. Zhigilei, Phys. Rev. B **66**, 115404 (2002).

[66] X. W. Zhou, H. N. G. Wadley, R. A. Johnson, D. J. Larson, N. Tabat, A. Cerezo, A. K. Petford-Long, G. D. W. Smith, P. H. Clifton, R. L. Martens, and T. F. Kelly, Acta Mater. **49**, 4005 (2001).

[67] L. D. Landau and E. M. Lifshitz, *Statistical Physics: Part I*, 3rd ed. (Butterworth-Heinemann, Oxford, 1999).

[68] L. D. Landau and E. M. Lifshitz, *Mechanics*, 3rd ed. (Pergamon, Oxford, 1976).

[69] G. Paltauf and P. E. Dyer, Chem. Rev. (Washington, D.C.) **103**, 487 (2003).

[70] J. R. Morris and X. Song, J. Chem. Phys. **116**, 9352 (2002).

[71] *Smithells Metals Reference Book*, 7th ed., edited by E. A. Brandes and G. B. Brook (Butterworth-Heinemann, London, 1998).

[72] L. V. Zhigilei and B. J. Garrison, Appl. Surf. Sci. **127−129**, 142 (1998).

[73] A. G. Zhidkov, L. V. Zhigilei, A. Sasaki, and T. Tajima, Appl. Phys. A: Mater. Sci. Process. **73**, 741 (2001).

[74] L. V. Zhigilei, E. Leveugle, B. J. Garrison, Y. G. Yingling, and M. I. Zeifman, Chem. Rev. (Washington, D.C.) **103**, 321 (2003).

[75] D. J. Evans, Phys. Rev. A **28**, 1016 (1983).

[76] N. W. Ashcroft and N. D. Mermin, *Solid State Physics* (Holt, Rinehart and Winston, New York, 1976).

[77] X. Y. Wang, D. M. Riffe, Y.-S. Lee, and M. C. Downer, Phys. Rev. B **50**, 8016 (1994).

[78] S. I. Anisimov and B. Rethfeld, Proc. SPIE **3093**, 192 (1997).

[79] C. Schäfer, H. M. Urbassek, L. V. Zhigilei, and B. J. Garrison, Comput. Mater. Sci. **24**, 421 (2002).

[80] R. H. M. Groeneveld, R. Sprik, and A. Lagendijk, Phys. Rev. B **51**, 11 433 (1995).